Nanoscale

Accepted Manuscript

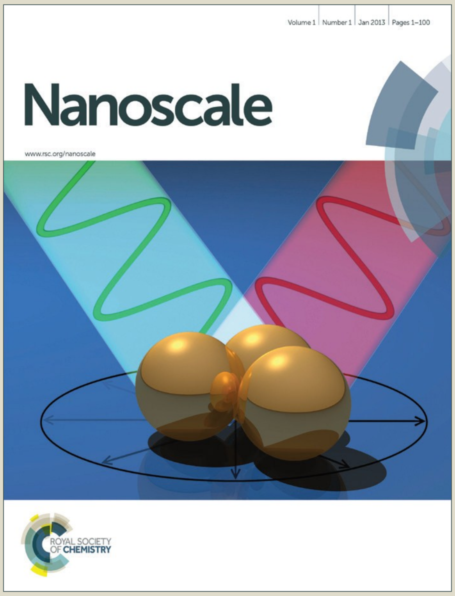

ROYAL SOCIETY OF CHEMISTRY

www.rsc.org/nanoscale

Synthesis, structural and electrochemical properties of sodium nickel phosphate for energy storage devices

Manickam Minakshi[1,*] David Mitchell[2], Rob Jones[3], and Feraih Alenazey[4]
[1]*School of Engineering and Information Technology, Murdoch University, Murdoch, WA 6150,* ***Australia***
[2]*Electron Microscope Centre, Australian Institute for Innovative Materials, Innovation Campus, University of Wollongong, North Wollongong, NSW 2500,* ***Australia***
[3]*Centre for Materials and Surface Science, La Trobe University, Bundoora, VIC 3086,* ***Australia***

[4]*Energy Research Institute, King Abdulaziz City for Science and Technology, Riyadh 11442,* **Saudi Arabia**
Teeraphat Watcharatharapong, Sudip Chakraborty, and Rajeev Ahuja
Department of Physics and Astronomy, Uppsala University, ***Sweden***

Abstract

Electrochemical energy production and storage at large scale and low cost, is a critical bottleneck in renewable energy systems. Oxides and lithium transition metal phosphates have been researched for over two decades and many technologies based on them exist. Much less work has been done investigating the use of sodium phosphates for energy storage. In this work, the synthesis of sodium nickel phosphate at different temperatures is performed and its performance evaluated for supercapacitor applications. The electronic properties of polycrystalline $NaNiPO_4$ polymorphs, triphylite and maricite, *t*- and *m*-$NaNiPO_4$ are calculated by means of first-principle calculations based on Spin-polarized Density Functional Theory (DFT). The structure and morphology of the polymorphs were characterized and validated experimentally and it is shown that the sodium nickel phosphate ($NaNiPO_4$) exists in two different forms (triphylite and maricite), depending on the synthetic temperature (300 – 550 ^oC). The as-prepared and triphylite forms of $NaNiPO_4$ *vs.* activated carbon in 2M NaOH exhibit the maximum specific capacitance of 125 F g^{-1} and 85 F g^{-1} respectively, at 1 A g^{-1} ; both having excellent cycling stability with retention of 99 % capacity up to 2000 cycles. The maricite form showed 70 F g^{-1} with a significant drop in capacity after just 50 cycles. These results reveal that the synthesized triphylite showed a high performance energy density of 44 Wh Kg^{-1} which is attributed to the hierarchical structure of the porous $NaNiPO_4$ nanosheets. At a higher temperature (> 400 ^{o}C) the maricite form of $NaNiPO_4$ possesses a nanoplate-like (coarse and blocky) structure with a large skewing at the intermediate frequency that is not tolerant of cycling. Computed results for the sodium nickel phosphate polymorphs and the electrochemical experimental results are in good agreement.

*** M. Minakshi (🖂)** E-mail: minakshi@murdoch.edu.au

1. Introduction

Alternative sources of energy will be an increasing part of the energy economy in the coming years. Energy storage systems are required in order to store the energy from renewable sources which is very intermittent. Electrochemical capacitors have been considered as an alternative power source, since they have higher power density and a longer life cycle, thereby sustaining higher current rates than traditional secondary batteries [1]. Supercapacitors are devices in which electrical charge arises from the accumulation of free ions on the surface of an electrode. Recently, paper-based flexible supercapacitor that suits the requirement for flexibility in portable electronics has also been widely reported [2-5]. In supercapacitors, the charge is stored electro-statically (non-faradaically) at the interfaces of the capacitor electrodes [6]. Non- faradaic processes are utilized in electrical double-layer (EDL) capacitors, which store energy based on the charge separation at a carbon electrode/ electrolyte interface. On the other hand, a faradaic process, due to redox (chemical) reactions, takes place at the electrode materials (such as conducting polymers, metal oxides, molybdates or phosphates) [6]. The latter group is termed pseudocapacitors, in that the electrical energy is stored by fast surface intercalation /de-intercalation reactions. Pseudo-capacitor materials, including transition metal oxides, such as RuO_2, MnO_2, NiO, Co_3O_4, Fe_3O_4, and electrical conducting polymers, such as polyaniline (PANI) and polypyrrole (PPy), are widely used [7-13]. Ruthenium oxide (RuO_2) has been widely investigated as a promising candidate because of its better conductivity and high specific capacitance. However, its large-scale application is limited by the high cost and scarcity of Ru [8]. At present, the environmentally- benign transition metal oxides, such as MnO_2, NiO, Co_3O_4 and Fe_3O_4, have been found to exhibit excellent redox activity and are readily available; thus, a high energy storage capacity can be obtained at relatively low cost [8]. In contrast, the poor electrical conductivity and slow response of conducting polymer materials results in low power densities and poor stability

[13]. As a solution, these materials are usually deposited on highly conductive carbon substrates to improve conductivity, as well as to achieve high capacitance.

Next to the oxides and hydroxides, transition metal phosphates and molybdates offer excellent performance in terms of structural stability, energy efficiency, safety and environmental inertness [14-16]. The ordered olivine structure, with general formula $LiMPO_4$ (M = Ni, Fe, Co or Mn) has been extensively studied as a cathode material in battery systems. These compounds contain tetrahedral anion structure units $(XO_4)^{n-}$ with strong covalent bonding, generating oxygen octahedral sites occupied by other metal ions [17]. Among the several metal atom substitutions, lithium-iron and lithium-manganese phosphates have been recognised as promising cations in the olivine structure. This is mainly due to low cost, environmental inertness, cycling stability and a high degree of reversibility.

Lithium reserves are located in remote regions of the world and may not be sufficient to address future global needs. Hence, substitution with cheaper and more ubiquitous sodium is a potentially attractive alternative to lithium-based olivine [18]. Our work here develops an important novel energy storage cathode material based on an affordable, globally available element: sodium. Until now, research into the sodium analogue, sodium iron phosphate ($NaFePO_4$), for battery systems has received limited attention with reports stating that these materials are not suitable for such applications [19]. This is due to FeO_6 octahedral lacking a diffusion channel for the insertion/extraction processes, making it electrochemically inactive. In this work, we have studied the synthetic steps and morphology of $NaNiPO_4$, using the highly conductive Ni cation in sodium analogue, in an aqueous electrolyte. This phase does have a reversible sodium insertion process. To the best of our knowledge, this is the first report on the development of $NaNiPO_4$ polymorphs *vs.* activated carbon as an aqueous asymmetric capacitor. The main objective of this study is to synthesize sodium nickel phosphate that possesses improved electrochemical performance, high power and energy density, and to utilize this material for supercapacitor applications. In this paper, we report the facile synthesis of both the triphylite and maricite forms of $NaNiPO_4$. The as-prepared material forms nanosheets while triphylite and maricite forms nanorods and plates, respectively. The triphylite form facilitates the mobility of ions from the electrolyte into the crystal structure, while the maricite form has unviable diffusion pathways resulting in poor cycling stability. The low temperature (as-prepared and triphylite) materials showed an excellent performance, with a maximum specific capacitance of 125 F g^{-1}. To understand the role of the structure of $NaNiPO_4$ in the faradaic redox reactions, we have performed electronic structure calculations for the triphylite (*t*) and maricite (*m*) polymorphs through the theoretical study using density functional theory (DFT).

Computational methods

The ground state electronic properties of *m* and *t* - $NaNiPO_4$ are obtained using the first-principle calculations based on spin-polarized Density Functional Theory (DFT), as implemented in Vienna Ab-initio Simulation Package (VASP) [20] package. The Projector-Augmented Wave (PAW) approach is applied to treat the core and valence electrons separately. To obtain accurate results, the semi core *p* states are included for Na ($2p^6$ $3s^1$) and Ni ($3p^6$ $4s^2$ $3d^8$) whereas the valence electron configurations of P and O are $3s^2$ $3p^3$ and $2s^2$ $2p^4$, respectively. The generalized gradient approximation proposed by Perdew, Burke and Ernzerhof (PBE) [21] is employed in all calculations to approximate the exchange-correlation term in the Kohn-Sham equation. The local density approximation (LDA) and the generalized gradient approximation (GGA) are very robust and successful methods that can effectively anticipate the ground state electronic properties of materials. They are, however, not able to provide a reliable size of the band gap and to properly handle self-interaction errors, especially, for d-localized electrons. In this regard, the hybrid functional was introduced to overcome this well-known shortcoming of PBE functional and is believed to be the most robust method to improve the accuracy of a calculated band gap. The hybrid functional (HSE06), proposed by Heyd, Scuseria, and Ernzerhof (HSE06), [22] incorporating a mixed Hartree - Fock (HF) and the PBE exchange functional, was used.

It can be expressed as the following equation (1)

$$E_{xc}^{HSE} = \alpha E_{x}^{HF,SR}(\omega) + (1-\alpha)E_{x}^{PBE,SR}(\omega) + E_{x}^{PBE,LR}(\omega) + E_{c}^{PBE} \qquad (1)$$

where α is a mixing parameter, ω is a controlling parameter for short-range interactions, $E_x^{PBE,SR(LR)}$ denotes a short range (long range) component of the PBE exchange energy, and E_c^{PBE} represents the PBE correlation energy. The default value for α in the HSE06 functional 0.25, was used in this work.

In the PBE calculations, a energy convergence threshold of 650 eV and 6 × 4 × 2 *k*-mesh gamma-centered grid were sufficient to converge the total energies to less than 1 meV/atom. For the hybrid-functional calculations, the same energy cutoff was used, but the *k*-mesh was reduced to 3 × 2 × 1 in order to reduce the computational expense. The DFT-D2 method proposed by Grimme [23] was used to calculate the van der Waal interactions. All structures were optimized using with four formula units (28 atoms) of $NaNiPO_4$ are fully optimized using a conjugate-gradient (CG) algorithm converging when the total energy differences and the residual Hellmann-Feynman forces were below 0.01 meV and 1meV/Å, respectively. The geometry optimization for all the structures are performed in both Ferromagnetic (FM) and Antiferromagnetic (AFM) configuration to find the lowest energy structures and are found to have the total energy difference approximately 6.6 and 8.4 meV per formula unit (f. u.) for maricite and triphylite structures, respectively. The local magnetic moments are determined from the projection of the magnetization density onto a Wigner-Seitz sphere of each atom.

2. Experimental

$Ni(OOCCH_3)_2.4H_2O$ (2.073 g), $Na(OOCCH_3).3H_2O$ (1.134 g), $NH_4H_2PO_4$ (0.958 g) and urea (0.5 g) were used as precursors for the synthesis of sodium nickel phosphate. The masses used correspond to equivalent molar ratios of $NaNiPO_4$. Urea was used as a source of fuel. All precursors were dissolved in distilled water (20 mL) with continuous. Aqueous ammonia was added to maintain the pH at ~ 8. The resulting solution was then placed on hot plate at 200 ˚C until dehydrated. The resultant solid was transferred to muffle furnace and the temperature raised to 300 ˚C. After 10 minutes, decomposition with gradual release of gases was observed. The final foamy product was ground using an agate mortar and pestle was termed "as-prepared / low temperature" and used for further characterization. The triphylite and maricite polymorphs were prepared by calcining this product at 400 and 550 °C, respectively, for 6 h.

The structural characterization of $NaNiPO_4$ powder was carried out with a Phillips Powder Diffractometer equipped with a Cu Kα source operating at 35 mA and 40 kV. Raman spectra were measured using a Nicolet 6700 FT-IR spectrophotometer equipped with a CaF_2 beam splitter, at a resolution of 8 cm^{-1}. X-ray photoelectron spectra were acquired using a Kratos AXIS Nova spectrometer (Kratos Analytical Ltd, U.K.) equipped with a monochromated Al Kα radiation source (1486.6 eV) operating at 150 W. Survey spectra were recorded at 1 eV/step and pass energy of 160 eV. Higher-resolution spectra acquired for selected photoemissions were recorded at 0.1 eV/step and a pass energy of 20 eV. To correct for the artificial increase in binding energy occurring as a result of the accumulation of surface charge during the acquisitions, all spectra were shifted so that the hydrocarbon component of the C 1s spectrum was at 285.0 eV. The surface morphologies of the materials were imaged at high magnification using a Zeiss Neon 40EsB focussed ion beam-scanning electron microscope (FIB-SEM). The nanostructure and lattice imaging of the $NaNiPO_4$ materials were characterized by transmission electron microscopy (TEM), high-resolution TEM (HRTEM), using a JEOL ARM200F TEM operated at 200 kV. The surface areas and porosities were measured by N_2 adsorption-desorption using a Micromeritics Tristar II analyser. Before analysis, the samples were degassed at 100 °C overnight.

For electrochemical measurement, the electrode was prepared by mixing $NaNiPO_4$ (75 wt %), carbon (acetylene) black (15 wt. %) and PVDF (10 wt. %) with 0.4 mL of NMP to make a slurry. The effects of acetylene black as conductive additive and PVDF as polymeric binder contents on the performance of a composite cathode has been studied and detailed in electronic supplementary information (ESI), Fig. S1. The slurry was coated on a small sheet of graphite (area of coating, 1 cm^2). The remainder of the graphite strip was masked using an insulation film to obtain a coated surface area of 1 cm^2 exposed to the electrolyte. The loaded active material was 2 mg in each case. To prepare the active negative electrode material, activated carbon (AC) (90 wt. %) and PVDF (10 wt. %) were used. A full cell ($AC||NaNiPO_4$) was fabricated by using a polypropylene separator. The cyclic voltammetry and galvanostatic charge-discharge studies of the composites were carried out using SP-150, Bio-Logic Science Instruments in 2 M NaOH electrolyte at room temperature.

3. Results and Discussion

(a) Crystal structure and density of states of $NaNiPO_4$ – theoretical studies

The crystal structures of *m*- and *t*-$NaNiPO_4$ belong to *Pnma* space group (No. 62) similar to *Pmnb* but their *a* and *c* unit vectors are just interchanged. From the structural optimizations using aforementioned methods, the crystal structure parameters are showed in Table 1. Both PBE and HSE06 hybrid (exchange correlation) functionals are used to optimize *m*-$NaNiPO_4$ and *t*-$NaNiPO_4$ to obtain the minimum energy configuration and to further explore the electronic structure. Due to the effect of introducing Hartree - Fock method (HF) exchange functional, the strengthening bonds and stronger electron localization could be observed leading to the shrink of cell volume. Therefore, the PBE lattice parameters in maricite form are more consistent with the experiment of Senthilkumar *et al.* in which a=5.0036 Å, b=6.7373 Å, c=8.7735 Å, and volume=297.5 Å^3 were reported [24]. From our hybrid calculation, the reliable band gaps of *m*- and *t*-$NaNiPO_4$ are 4.94 and 5.03 eV, respectively, which are larger than those obtained from PBE (0.76 and 0.86 eV, respectively). Clearly, this reflects the presence of strong electron localization in $NaNiPO_4$. Moreover, altering the site of Na and Ni causes the triphylite form creating more space for Na ions to occupy and intercalate along one-dimensional [010] channel in its orthorhombic framework, which is an essential factor for energy storage host materials. From the spin-polarized calculation perspective, the antiferromagnetic (AFM) coupling on Ni has been found to be energetically favourable than ferromagnetic (FM) at zero temperature and both AFM structures with different magnetic orderings can lead to the total energy difference approximately 7 – 30 meV/f .u.

In Figure 1, the optimized crystal structure of both polymorphs are illustrated along with the stable magnetic orientation on Ni atoms, in which magnetic moments in any *xz* planes are likely to point in same directions. The magnitudes of Ni-ion spin moments in *m*- and *t*-$NaNiPO_4$ are found to be 1.763 and 1.760 μ_B, respectively. From the total energies of maricite and triphylite structures in their AFM configurations, it reinforces that the former has higher stability with total energy difference of 29.62 meV/f. u. However, due to the lack of diffusion channel for sodiation it resulted in entrapment of Na^+ ion that exhibits poor reversibility and fast capacity fading. In the case of the triphylite structure, it is expected to provide higher power and energy densities through the presence of diffusion channels. To have a profound understanding regarding the inherent electronic structures, density of states (DOS) are calculated using hybrid functional as displayed in Figure 2. It reveals that, besides a little gap difference, their total DOS are similar. Although the DOS for *m*-$NaNiPO_4$ near the Fermi level has more states compared to the triphylite and has a smaller band gap which can allow the higher amount of electrons to drift thermally across, these should not make an explicit difference on their inherent electrical conductivity. Since the high storage capability corresponds to the intrinsic electronic conductivity, it could imply that regardless the presence of Na-diffusion channels, the observed high performance for triphylite sample does not originate from its electrical conductivity itself. In order to explore the individual contributions of each atom regarding electronic density of states that lead to the band gap, the projected density of states (PDOS) of both structures are calculated as depicted in Figure 3. It is found in both PDOS that *2p*-electrons of oxygen atoms contribute mostly in valence band region and hybridize with *3d*-electrons of Ni atoms, while the conduction band is mostly contributed by *3d*-electrons of Ni atoms.

Figure 4 shows the electron occupancy of Ni in e_g and t_{2g} states for *m*- and *t*-$NaNiPO_4$, using HSE06 exchange correlation functional. It shows in both cases that the energy of t_{2g} bands is higher than the other in an octahedral crystal field. The Jahn-Teller distortion (compression) can be observed among these two structures and are found more explicitly in maricite as an evidence of the broken degeneracy of d_{z^2} and $d_{x^2-y^2}$. For this structure, we have found that e_g bands identically have *d*-orbital half-filling, each of them contains a single electron, which indicates that Ni ions in both forms possess 2+ states in the high-spin $t_{2g}^6 e_g^2$ configurations ($3d^8$). This leads to the conclusion that the high-spin Ni^{2+} can be observed when $NaNiPO_4$ in both forms are in fully discharging state. Additionally, the presence of Ni^{3+} could be possibly envisaged at the end of charging cycle. This prediction is in reasonable agreement with the experimental (electrochemical characterization) finding that the host materials can accommodate states of $Ni^{2+/3+}$which is discussed in the following section.

(b) Experimental measurements of NaNiPO$_4$

Physical Characterization

The X-ray diffraction patterns of sodium nickel phosphate (NaNiPO$_4$) synthesized at different temperatures (a) 300 ^{o}C, (b) 400 ^{o}C and (c) 550 ^{o}C are shown in Fig. 5. The crystal structures of these materials all indexed to an orthorhombic framework belonging to *Pnma* space group, built from NiO$_6$ octahedral and PO$_4$ tetrahedral units having corner-sharing and edge-sharing arrangements. The precursors synthesized at 300 ^{o}C for 10 min shows few diffraction peaks. When this sample is calcined at 400 ^{o}C for 6 h and the pattern matches that of triphylite NaNiPO$_4$ (olivine form). In the triphylite form, the sodium (Na) occupies *M*1 (4a) site while Ni occupies *M*2 (4c) site which is analogous to olivine structure [25]. When the temperature is increased to 550 ^{o}C for 6 h, the pattern closely matches that of maricite NaNiPO$_4$. In the maricite form, the distribution arrangement is reversed, with Ni occupying *M*1 (4a) site and Na occupying *M*2 (4c) site, as illustrated in the crystal structure shown in Fig. 1. The high intensity and sharp peaks indicate that the synthesized NaNiPO$_4$ is highly crystalline with long-range order. Overall, the X-ray diffraction pattern reveals the difference in crystal structure with respect to the synthesis temperature. The results closely match the work reported by Barpanda et al. [25]. The difference in structure is confirmed with the Raman spectra in Fig. 6. Two strong bands at 895 and 960 cm^{-1} were observed for the material produced at 400 ^{o}C material while only one strong band at 1000 cm^{-1} is observed for that prepared at 550 ^{o}C. All the peaks are symmetric and asymmetric stretching modes of the P – O bonds. The bands are assigned with reference to the reported assignments of the spectra of LiNiPO$_4$ and other phosphate structures [26-27]. The difference seen in position of the symmetric stretching vibration in NaNiPO$_4$ at 550 ^{o}C compared with that at 400 ^{o}C is a function of synthetic temperature and illustrates the formation of new crystal structure (maricite).

The surface morphology of the $NaNiPO_4$ nanostructure was investigated by transmission and scanning electron microscopy (TEM and SEM). Figure 7a-c shows the as-prepared sample (synthesized at 300 ^{o}C for 10 min). The particles (Fig. 7a) are blocky and are comprised of agglomeration of nanocrystals. Bright field scanning transmission electron microscopy (STEM) and STEM secondary electron imaging (Figs. 7b and c) showed agglomerates with a striated texture. STEM secondary electron imaging (Fig. 7c) indicated that this was a hierarchical structure of $NaNiPO_4$ nanosheet like particles stacked on top of each other. These interspaces/layers give improved access to ions from the electrolyte, creating more reaction sites and thus improving the electrochemical performance and utilization of the active material. The selected area diffraction pattern of this region (Fig. S2a) confirmed that the particles were polycrystalline. Diffuse rings were present in the pattern, suggesting that an amorphous component was also present. Figures 7d-e show the sample calcined at 400 ^{o}C for 6 h, revealing a nanorod like morphology varying from 100 nm to 500 nm in length. These nanorods attach to adjacent rods forming clusters. The material is composed entirely of large dense rod-like crystals suggesting complete recrystallization forming triphylite which is consistent with the XRD pattern shown in Fig. 7b. The selected area diffraction pattern (Fig. S2b) is ostensibly, that of a single crystal of $NaNiPO_4$. No diffuse rings from the amorphous phase seen at lower temperature are present, suggesting a completely crystalline phase. Figures 7f-g shows a TEM image for the sample calcined at 550 ^{o}C for 6 h, revealing very large plate-like crystals ranging from 300 nm to 1 µm. The selected area diffraction pattern (Fig. S2c) is from a single large particle and showed intense diffraction spots consistent with the highly crystalline maricite form of $NaNiPO_4$. Figure 8 shows SEM micrographs of $NaNiPO_4$ synthesized at different temperatures. Figure 8a-b show a well-defined nanosheet-like structure seen for the as-prepared material (300 ^{o}C), in agreement with the aforementioned TEM (Fig. 7a-c). At higher temperatures the nanosheet-like morphology has changed to rod- (400 ^{o}C) and plate-like (550 ^{o}C) rounded crystals. From Figs. 8c-d, it is apparent that calcination at higher temperature produces denser material. Due to surface area considerations alone, this would result in a less electrochemically active phase at the higher temperature (Fig. 8d 550 ^{o}C). Chemical analysis using energy dispersive x-ray microanalysis (EDS in Fig. 8e) confirmed that all phases were free from impurities and contained only Na, Ni, P, and O.

As the electrochemical performance of the sodium nickel phosphate ($NaNiPO_4$) synthesized at different temperatures may in part depend on the specific area and pore volume, the pore structures of the samples were measured from N_2 adsorption – desorption isotherms. Typical isotherm curves are displayed in Fig. 9 with a pore size distribution shown in the inset. The pore size distribution for all three samples synthesized at 300, 400 and 550 ^{o}C are quite uniform having small mesopores with a size around 3 nm. The samples synthesized at the lower temperature yield a type IV isotherm [28], with hysteresis loops at moderate relative pressure. In contrast the higher temperature materials yield a type II isotherm. The number of small mesopores present in the partially amorphous agglomeration of nanocrystals (300 ^{o}C) is found to be higher (shown in the inset of Fig. 9) than that of nanorods (400 ^{o}C) and aggregates of plate like (550 ^{o}C) crystals. The 300 ^{o}C sample has a BET surface area of 8.72 m^2/g, and the ratio of mesopore to micropore volume is 19, while the BET values of 400 ^{o}C and 550 ^{o}C are 6.54 m^2/g, 15.5 m^2/g and the ratio are 15 and 11, respectively. This means the surface area and number of mesopores are greater in the 300 ^{o}C material than in the triphylite and maricite form of $NaNiPO_4$. Hence, it is expected that the as-prepared sample at 300 ^{o}C will show enhanced electrochemical energy storage.

(c) Electrochemical Characterization

I. *NaNiPO$_4$ – single electrode studies*

The electrochemical redox behaviour of the three NaNiPO$_4$ materials was characterized by cyclic voltammetric and galvanostatic measurements in 2M NaOH electrolyte (Figs. 10−12). Figure 10a-c shows the redox behavior of NaNiPO$_4$ as a single electrode at various sweep rates between 0 and 0.6 V for the synthesis temperatures of 300, 400 and 550 ^{o}C, respectively. The CV plots show a well-defined oxidation (A$_1$) and reduction (C$_1$) peaks during the anodic and cathodic scans at 0.57 and 0.45 V *vs*. the standard electrode (Hg/HgO) respectively. The integrated areas of the peaks are proportional to the sweep rates reflecting fast redox reactions suitable for energy storage applications. The shape of the CV curves clearly implies that faradic reactions (pseudocapacitive in nature) occurred during the processes and the obtained behaviour is typical of an equivalent battery-type material reported in the literature [16]. Irrespective of the synthesis temperature, all three samples exhibit an identical pair of redox peaks (A$_1$ and C$_1$) located at the same potential which is a characteristic of the NaNiPO$_4$ material. However, the intensities of the redox peaks are higher for triphylite (Fig. 10b) and lower for maricite form (Fig, 10c) of NaNiPO$_4$. A similar well-defined redox behavior has been observed for nickel phosphates in aqueous solutions [24, 29]. Based on this, these peaks can be ascribed to extraction and reversible intercalation of sodium from/into the NaNiPO$_4$ polymorphs resulting in Ni^{3+} and Ni^{2+} ions of oxidation and reduction respectively. The electrochemical performance of activated carbon was investigated for its suitability as a negative electrode. A typical electric double-layer capacitive type characterized by nearly box shaped curve without any redox peaks is shown in Fig. 10d [14-16]. This behaviour corresponds to an adsorption / desorption mechanism of OH$^-$ ions from the NaOH electrolyte. However, for the positive electrode NaNiPO$_4$, a distinct pair of redox peaks which is a deviation from the box shaped curve has occurred. The profiles for the two materials are compared in Fig. 10d. It can be inferred from these single cell characteristics that the useful working voltage for negative activated carbon electrode is 1.0 V while that for the positive $NaNiPO_4$ electrode it is 0.6 V, resulting in a potential of 1.6 V for a full cell system. This hybrid cell ($NaNiPO_4$ *vs*. Activated carbon) has been investigated for practical applications. From the single cell characteristics, it is inferred that to maintain the charge balance of the hybrid cell, the optimal mass ratio between the activated carbon and $NaNiPO_4$ electrodes ($k = m_+/m$) was estimated to be 1.05. The mass of the positive and negative electrode material was 2.0 and 2.1 mg, respectively.

The electrochemical performance of $NaNiPO_4$ *vs*. Activated carbon was evaluated as capacitive electrodes in an asymmetric system using an aqueous 2M NaOH electrolyte. The capacitance (C) and energy density (E) of the hybrid cell were calculated using the following equations (2-3):

$$C\ (\mathrm{F\ g^{-1}}) = I\ \Delta t / m\ \Delta V \qquad (2)$$

$$E\ (\mathrm{Wh\ Kg^{-1}}) = \tfrac{1}{2}\, C\ \Delta V^2 \qquad (3)$$

Where I *(A)* is the constant discharge/charge current, Δt *(sec)* is the time elapsed for the discharge /charge cycle, m *(g)* is the mass of the active material i.e. $NaNiPO_4$ (or) activated carbon and ΔV *(V)* is the working voltage window.

II. Asymmetric supercapacitor AC||$NaNiPO_4$ – two electrode configuration

Figure 11 shows voltage *vs*. time (galvanostatic charge-discharge) curves at different current densities for $NaNiPO_4$ electrodes synthesized at different temperatures and the corresponding specific capacitances are tabulated in Table 2. The calculated specific capacitance for the as-prepared sample (300 °C) at various current densities 1, 2, 3, 5, 7 and 10 A g^{-1} are 125, 98, 66, 54, 40 and 30 F g^{-1} respectively. The linear relationship between the imposed current rate and the obtained specific capacitance indicate that the as-prepared electrode is controlled by the diffusion process and redox reactions taking place in the discharge process. The IR drop is not significant even at higher current densities implying the material is sustainable even at higher current rates - a prerequisite for capacitors. This is supported with electrochemical impedance spectroscopy (EIS) analysis and discussed later in the section. Figure 11a shows that the specific capacitances were largely retained even at a higher current density of 10 A g^{-1}. At higher current rates (> 5 A g^{-1}) the charge-discharge curves are symmetrical corresponding to adsorption and desorption of OH^- ions from the electrolyte on the $NaNiPO_4$ particles. However, at a lower scan rate of 1 A g^{-1}, the non-linearity of the curve indicates the influence of redox reaction corresponding to $Ni^{2+/3+}$ [16]. The observed higher capacitance of 125 F g^{-1} at this low scan rate could include a contribution from pseudocapacitance. The $NaNiPO_4$ *vs*. AC hybrid device combines the intercalation mechanism and electric double-layer capacitance that endows it with a high specific capacitance [30]. In the case of the material calcined at 400 ^{o}C (Fig. 11b) at various current densities 1, 2, 3, 5, 7 and 10 A g^{-1} the obtained capacitances are 85, 60, 40, 38, 25 and 10 F g^{-1} respectively. When compared to those of the as-prepared sample, the available capacitance of triphylite $NaNiPO_4$ is 30 – 40 % lower. This could be due to recrystallization, the available surface area has been reduced to 25%. It may also be due to ion diffusion is limited by large dense rod-like crystals having a larger grain size. The samples calcined at 550 ^{o}C, maricite $NaNiPO_4$, in Fig. 11c showed the poorest behavior of the three materials studied. At current densities of 1, 2, 3, 5, 7 and 10 A g^{-1} the obtained capacitances shown in Fig. 11d are 70, 55, 33, 23, 8 and 4 F g^{-1} respectively. The plate-like morphology with very less accessible surface area of only 45% resulted to have lower capacitances. A similar trend of electrochemical profile is also observed (in Fig. 12) when tested under potentiodynamic conditions for the asymmetric capacitor AC||$NaNiPO_4$ examined at various sweep rates ranging from 1 to 20 mV s^{-1}. The symmetric nature of the CV curves (in Fig. 12a) possessing the reversible current response of high peak (A_1 and C_1) currents at various scan rates indicates the ideal electrochemical double layer capacitor (non-faradaic) behaviour and a contribution from the faradic reactions for the as-prepared sample (300 ^{o}C). In the case of the $NaNiPO_4$ calcined at 400 ^{o}C (Fig. 12b) exhibits a well-defined anodic (A_1) and cathodic (C_1) peak attributed mainly to a pseudo-capacitance process. For the maricite $NaNiPO_4$ calcined at 550 ^{o}C in Fig. 12c shows sluggish kinetics with a lower current response. At a higher scan rate (20 mV s^{-1}) only a fraction of electrode surface may be accessible to the electrolyte thus the redox peaks are ill-defined. The specific capacitance decreased with an increase in sweep rates (in Table 3), however, at a relatively high sweep rate of 20 mV s^{-1}, the available specific capacitance is still retained at 52 F g^{-1} which is about three-fold higher than the maricite counterpart which is 19 F g^{-1}. This indicates the excellent rate capability of the triphylite $NaNiPO_4$.

III. Electrochemical impedance spectroscopy and X-ray photoelectron spectroscopy study

To further illustrate the differences seen in the triphylite and maricite crystal structure upon the electrochemical performance of $NaNiPO_4$, electrochemical impedance spectroscopy (EIS) experiments and x-ray photoelectron spectroscopy (XPS) are carried out and the results are shown in Figures S3 and S4.

The Nyquist plot in Fig. S3 displays the measurements made from the $NaNiPO_4$ synthesized at different temperatures and the corresponding equivalent circuit is shown in the inset. A different electrochemical process for the $NaNiPO_4$ electrodes can be clearly distinguished in the spectra. The sample synthesized at 300 ^{o}C showed a fused semicircle with no conspicuous difference in the low and high-frequency region and a straight line is observed in the low-frequency region. The intercept on the real axis (electrolyte solution ohmic resistance; R_s) [31] and the diameter of the semicircle (charge transfer non-ohmic resistance; R_{ct}) [32] are about 5 Ω and 2 Ω, respectively. The slope of the straight line closer to 90^o related to the high diffusion of OH^- ions from the NaOH electrolyte into the $NaNiPO_4$ indicate that the material is associated with both faradaic and non-faradaic behavior, a characteristic nature of the pseudocapacitor, yielding a low Warburg resistance value (W_o) [33]. For the sample synthesized at 400 ^{o}C, more or less separated semicircles appeared at high and low frequency regions. The high frequency flattened semicircle (R_s) of 9 Ω reflects the relative higher resistance of ionic diffusion in the $NaNiPO_4$ surface layer of the electrode. The intermediate frequency with a large skewing (R_{ct}) of 13 Ω is related to the charge transfer resistance in the electrode/electrolyte interface, and the inclined angle of about 45^o to the real axis is generally attributed to lower ionic diffusion. A very similar electrochemical performance of asymmetric capacitor is also reflected in potentiostatic and galvanostatic experiments discussed in Figs. 11 and 12. R_{SEI} and C_{SEI} [34] represent the solid electrolyte interface layer on the surface of the activated carbon anodes, while C_{dl} [35] is the double layer of charge formed at the interface. For the sample synthesized at 550 ^{o}C, the diameter of the semicircle become widened, with R_s and R_{ct} values are of about 10 Ω and 35 Ω respectively, indicating that the contribution of pseudocapacitance is relatively lower than that for the other two samples synthesised at 300 ^{o}C and 400 ^{o}C. The near straight line in the low frequency region illustrates the higher Warburg resistance associated with the diffusion of electrolyte ions through adsorption in the bulk $NaNiPO_4$ is however accessible. Therefore, the improved electrochemical performance is attributed to the smaller charge transfer resistance and higher electronic conductivity owing to the triphylite structure.

XPS survey spectra (0 –1200 eV) of the $NaNiPO_4$ samples contained peaks associated with the elements Na, Ni, P, O, C, and N (not shown here). The atomic fractions of these elements are listed in Table S1. Only in the case of the triphylite sample, the measured atomic fractions of Na, Ni, P, and O are approximately equal to their stoichiometric values. Spectra recorded at higher energy resolution for the C 1s and O 1s regions of the samples prepared at

400 ^{o}C and 550 ^{o}C are show in Figs S4a-b and S4c-d, respectively. The C 1s spectra are each fitted to three components. The most intense of these is the component at lowest binding energy (BE), which is attributed to carbon atoms in hydrocarbon groups [36]. The BE of the second component in each is 1.3 - 1.6 eV higher than that of the hydrocarbon peak, and so is attributed to carbon atoms singly bonded to oxygen, in alcohol or ether functional groups. The BE of the third component is between 288.6 and 288.9 eV, which is within the range observed for O–C=O functional groups. The BEs of all spectra were shifted so that the hydrocarbon component is centred at 285.0 eV, to correct for energy shifts resulting from sample charging during irradiation. The O 1s spectrum for each sample is fitted to two component peaks, Fig. S4 c-d, centred at about 531.2 and 532. 3 eV. An additional component, at higher binding energy, is associated with the Na KLL Auger emission. The O 1s component at lowest BE is attributed to inorganic oxide species, such as phosphate. The second is attributed to organic species, such as C–O and O=C–O. The differences seen in the atomic fractions between the elements Na and Ni (Table S1) and the spectra corresponding to C and O explains the surface functionality on the triphylite and maricite crystal structures and that explain the variations seen in the electrochemical performances. The Ni 2p spectra acquired for these samples are all quite similar. The maximum in the $2p_{3/2}$ peak in each occurs between 855.9 and 856.3, which is within the range reported for Ni^{II} compounds [37].

IV. *Asymmetric supercapacitor AC||$NaNiPO_4$ – Long term cycling*

To evaluate the cycling stability of the device, the charge-discharge cycling of the $NaNiPO_4$ *vs*. Activated carbon cell was performed at a current rate of 2 A g^{-1} (Fig. 13). The as-prepared (300 ^{o}C) sample exhibits almost 100% capacitance retention after 2000 cycles. The charge-discharge curves are shown in the insets which are exactly superimposed for the 5th and 2000th cycles. Although, the triphylite sample (400 ^{o}C) exhibits a lower capacitance of 60 F g^{-1} but it too showed excellent cycling stability by retaining 100% of capacity after 2000 cycles. The charge discharge curves for the 1st and 2000th cycle (inset in Fig. 13b) have exactly the same shape and amplitude. The maricite form of $NaNiPO_4$ (550 °C) showed 70 F g^{-1} with a significant drop in capacitance after just 50 cycles (Fig. 13c) losing over 40% of the initial capacitance. These results confirm that the as-prepared and triphylite form of $NaNiPO_4$ shows excellent cycling stability and deliver high capacitance, illustrating that these materials are promising for energy storage applications. The nanosheets (as-prepared) and nanorod-like (triphylite) morphology having high aspect ratio allows for a shorter diffusion length of ions and maintain the structural stability for reversibility. However, maricite $NaNiPO_4$ crystal structure is not suitable for multiple cycling as depicted from the crystal and electronic structure of $NaNiPO_4$ polymorphs. The energy densities of as-prepared, triphylite and maricite form of $NaNiPO_4$ are 44, 32 and 25 Wh Kg^{-1} at power densities 265, 215, 175 W Kg^{-1}. A Ragone plot for the $NaNiPO_4$ samples is compared and the results are shown in Fig. S4. The triphylite $NaNiPO_4$ capacitor showed a superior performance to a maricite in the terms of energy and power densities. To understand the performance and potential of the devices presented here, we have also compared with the lithium-ion and sodium-ion capacitors based on activated carbon electrodes. The energy densities of the as-prepared and triphylite form of asymmetric $NaNiPO_4$ /AC sodium-ion capacitor (~ 40 Wh Kg^{-1}) is superior to that of an symmetrical AC/AC double layer capacitor (26 Wh Kg^{-1}) [1], AC/$NaNi_{0.33}Co_{0.33}Mn_{0.33}PO_4$ (13 Wh Kg^{-1}) [16], AC / $Li_4Ti_5O_{12}$ (34 Wh Kg^{-1}) [38], AC / $NiCo_2O_4$ (14 Wh Kg^{-1}) [39], AC/sodium titanate nanotubes (34 Wh Kg^{-1}) [40], AC/$Na_4Mn_9O_{18}$ (34.8 Wh Kg^{-1}) [41].

4. Conclusions

We have synthesized sodium nickel phosphate ($NaNiPO_4$) and explored the structural, morphology and electrochemical properties of the triphylite and maricite polymorphs. Structural studies confirm that the compound exists in two different forms, depending on the synthetic temperature. The as-prepared nanosheet materials showed a maximum capacitance of 125 F g^{-1} with 100% retention of capacity under charge/discharge cycling up to 2000 cycles. The calcined nanorods of the triphylite form showed a capacitance of 85 F g^{-1} with 100% retention during similar cycling. However, the coarse, blocky maricite form showed a lower capacitance of 70 F g^{-1} with a 40% drop in capacity after just 50 cycles. The poor performance may be due to a decrease in available surface area, hindering penetration of the electrolyte. The fabricated hybrid device utilises both redox reactions involving nickel ions and adsorption/desorption of OH^- ions in EDLC behavior. This resulted in high specific capacitance and energy density. This new $NaNiPO_4$ -based capacitor is promising and the performance is superior to that of an oxide and lithium-based phosphate materials. Our theoretical and experimental studies reveal that both the as-prepared and triphylite forms are more favourable for faradaic redox reactions to occur than maricite form.

Acknowledgements

This research was supported under ARC's Discovery Projects funding scheme (DP1092543). The views expressed herein are those of the authors and are not necessarily those of the Australian Research Council. This research used equipment funded by the Australian Research Council (ARC) – Linkage, Infrastructure, Equipment and Facilities (LIEF) grant LE120100104 located at the UOW Electron Microscopy Centre. TW would like to acknowledge Development and Promotion of Science and Technology Talents Project (DPST) and Thai Government. SC and RA would like to thank Carl Tryggers, ST and UP and VR. SNIC, HPC2N and UPPMAX are also acknowledged for the computing time.

References

1. J. Zhang, J. Jiang, H. Li, and X. S. Zhao, A high-performance asymmetric supercapacitor fabricated with graphene-based electrodes, Energy Environ. Sci. 4 (2011) 4009 – 4015.

2. H. Pang, Y.-Z. Zhang, Z. Ren, W.-Y. Lai and W. Huang, Amorphous nickel pyrophosphate microstructures for high-performance flexible solid-state electrochemical energy storage devices, Nano Energy 17 (2015) 339 – 347.
3. H. Pang, Y.-Z. Zhang, W.-Y. Lai, Z. Hu and W. Huang, Lamellar $K_2Co_3(P_2O_7)_2.2H_2O$ nanocrystals whiskers: High-performance flexible all-solid-state asymmetric micro-supercapacitors via inkjet printing, Nano Energy 15 (2015) 303 – 312.
4. Y-Z. Zhang, J. Zhao, J. Xia, L. Wang, W.-Y. Lai, H. Pang, and W. Huang, Room temperature synthesis of cobalt – manganese nickel oxalates micropolyhedrons for high-performance flexible electrochemical energy storage device, Sci. Reports 5 (2015) 8536.
5. Y-Z. Zhang, Y. Wang, T. Cheng, W.-Y. Lai, H. Pang, and W. Huang, Flexible supercapacitors based on paper substrates: a new paradigm for low-cost energy storage, Chem. Soc. Rev. 44 (2015) 5181 – 5199.
6. C. Liu, F. Li, L.-P. Ma, M.-M. Cheng, Advanced materials for energy storage, Adv. Mater. 22 (2010) E28 – E62.
7. Y-Z. Zhang, Y. Wang, Y.-L. Xie, T. Cheng, W.-Y. Lai, H. Pang, and W. Huang, Porous hollow CO_3O_4 with rhombic dodecahedral structures for high-performance supercapacitors, Nanoscale 6 (2014) 14354 – 14359.
8. Y. Wang, J. Guo, T. Wang, J. Shao, D. Wang, and Y.-W. Yang, Mesoporous transition metal oxides for supercapacitors, Nanomater. 5 (2015) 1667 – 1689.
9. L. Deng, J. Wang, G. Zhu, L. Kang, Z. Hao, Z. Lei, Z. Yang, Z.-H. Liu, RuO_2/graphene hybrid material for high performance electrochemical capacitor, J. Power Sources 248 (2014) 407 – 415.

10. G. Zhang, L. Ren, L. Deng, J. Wang, L. Kang and Z.-H. Liu, Graphene-MnO_2 nanocomposite for high performance asymmetrical electrochemical capacitor, Mater. Res. Bull. 49 (2014) 577 -583.
11. X.-H. Xia, J.-P. Tu, Y.-J. Mai, X.-L. Wang, C.-D. Gu, and X.-B. Zhao, Self-supported hydrothermal synthesized hollow Co_3O_4 nanowire arrays with high supercapacitor capacitance, J. Mater. Chem. 21 (2011) 9319 – 9325.
12. L. Wang, H. Ji, S. Wang, L. Kong, X. Jiang and G. Yang, Preparation of Fe_3O_4 with high specific area and improved capacitance as a supercapacitor, Nanoscale 5 (2013) 3993 – 3799.
13. P. Pieta, I. Obraztsov, F. D'Souza, and W. Kutner, Composites of conducting polymers and various carbon nanostructures for electrochemical supercapacitors, J. Electrochem. Soc., 2 (2013) M3120 – M3134.
14. R. Ramkumar and M. Minakshi, Fabrication of ultrathin $CoMoO_4$ nanosheets modified with chitosan and their improved performance in energy storage device, Dalton Trans. 44 (2015) 6158 – 6168.
15. C. Yang, L. Dong, Z. Chen and H. Lu, High-performance all solid-state supercapacitor based on the assembly of graphene and manganese (II) phosphate nanosheets, J. Phys. Chem. C. 118 (2014) 18884 – 18891.
16. M. Minakshi, D. Meyrick and D. Appadoo, Maricite ($NaMn_{1/3}Ni_{1/3}Co_{1/3}PO_4$) / Activated Carbon: Hybrid Capacitor, Energy & Fuels 27 (2013) 3516 – 3522.
17. A. K. Padhi, K. S. Nanjundaswamy, and J. B. Goodenough, Phospho-olivines as positive electrode materials for rechargeable lithium batteries, J. Electrochem. Soc. 144 (1997) 1188 – 1194.

18. P. Han, X. Han, J. Yao, L. Zhang, X. Cao, C. Huang and G. Cui, High energy density sodium-ion capacitors through co-intercalation mechanism in diglyme-based electrolyte system, J. Power Sources 297 (2015) 457 – 463.
19. A. Sun and A. Manivannan, Structural studies on $NaFePO_4$ as a cathode material for Na^+/Li^+ mixed-ion batteries, ECS Trans. 35 (2011) 3 – 7.
20. G. Kresse and D. Joubert, From ultrafast pseudopotentials to the projector augmented-wave method, Phys. Rev. B 59 (1999) 1778 – 1775.
21. J. P. Perdew, K. Burke and M. Ernzerhof, Generalized Gradient Approximation Made Simple, Phys. Rev. Lett. 77 (1996) 3865 – 3868.
22. J. Heyd, G. E. Scuseria and M. Ernzerhof, Hybrid functionals based on a screened Coulomb potential, J. Chem. Phys. 118 (2003) 8207 – 8215.
23. S. Grimme, Semiemprical GGA-type density functional constructed with a long-range dispersion correction, J. Comp. Chem. 30 (2006) 1787 – 1799.
24. B. Senthilkumar, K. V. Sankar, L. Vasylechko, Y.-S. Lee, and R. K. Selvan, Synthesis and electrochemical performances of maricite-$NaMPO_4$ (M = Ni, Co, Mn) electrodes for hybrid supercapacitors, RSC Adv. 4 (2014) 53192–53200.
25. M. Avdeev, Z. Mohamed, C. D. Ling, J. Lu, M. Tamru, A. Yamada and P. Barpanda, Magnetic structures of $NaFePO_4$ maricite and triphylite polymorphs for sodium-ion batteries, Inorganic Chem. 52 (2013) 8685 – 8693.
26. G. Butt, N. Sammes, G. Tompsett, A. Smirnova and O. Yamamoto, Raman spectroscopy of superionic Ti-doped $Li_3Fe_2(PO_4)_3$ and $LiNiPO_4$ structures, J. Power Sources 134 (2004) 72 – 79.
27. R. L. Frost and S. J. Palmer, Raman spectroscopy of stercorite $H(NH_4)Na(PO_4).4H_2O$ – A cave mineral from Petrogale cave, Madura, Eucla, Western Australia, Spectrochim. Acta Part A 79 (2011) 1215 – 1219.

28. K. S. W. Sing, D. H. Everett, R. A. W. Haul, L. Moscou, R. A. Pierotti, J. Rouquerol and T. Siemieniewska, Reporting Physisorption data for gas/solid systems with special reference to the determination of surface area and porosity, Int. Union of Pure and App. Chem. 57 (1985) 603 – 619.

29. M. Minakshi, P. Singh, D. Appadoo and D. E. Martin, Synthesis and characterization of olivine $LiNiPO_4$ for aqueous rechargeable battery, Electrochim. Acta 56 (2011) 4356 – 4360.

30. N. Yabuuchi, K. Kubota, M. Dahbi, and S. Komaba, Research development on sodium-ion batteries, Chem. Rev. 114 (2014) 11636 – 11682.

31. K. N. Allahar, D. Battocchi, G. P. Bierwagen and D. E. Tallman, Transmission line modelling of EIS data for a Mg-rich primer on AA 2024-T3, J. Electrochem. Soc. 157 (2010) C95 – C101.

32. Y. Zhang, C. Yuan, K. Ye, X. Jiang, J. Yin, G. Wang and D. Cao, An aqueous capacitor battery hybrid device based on Na-ion insertion-de insertion in λ-MnO_2 positive electrode, Electrochim. Acta 148 (2014) 237 – 243.

33. H-K. Song, Y.-H. Jung, K.-H. Lee and L. H. Dao, Electrochemical impedance spectroscopy of porous electrodes: the effect of pore size distribution, Electrochim. Acta 44 (1999) 3513 – 3519.

34. P. Mauracher and E. Karden, Dynamic modelling of lead/acid batteries using impedance spectroscopy for parameter identification, J. Power Sources 67(1997) 69 – 84.

35. M. Minakshi Sundaram, A. Biswal, D. Mitchell, R. Jones and C. Fernandez, Correlation among physical and electrochemical behavior of nanostructured electrolytic manganese dioxide from leach liquor and synthetic for aqueous asymmetric behavior, Phys. Chem. Chem. Phys. 18 (2016) 4711- 4720.

36. Thermo Scientific XPS Knowledge Base, Carbon
http://xpssimplified.com/elements/carbon.php

37. A. N. Mansour, Nickel Monochromated Al Kα XPS Spectra from the Physical Electronics Model 5400 Spectrometer, Surf. Sci. Spectra 3 (1994) 23921 – 246; ibid, 247–254; ibid, 255–262.86.

38. H. Kim, K.-Y. Park, M.-Y. Cho, M. – H. Kim, J. Hong, S.-K. Jung, K. C. Roh and K. Kang, High performance hybrid supercapacitor based on graphene wrapped $Li_4Ti_5O_{12}$ and activated carbon, ChemElectroChem. 1 (2014) 125 – 130.

39. R. Ding, L. Qi and H. Wang, An investigation of spinel $NiCo_2O_4$ as anode for Na-ion capacitors, Electrochim. Acta 114 (2013) 726 – 735.

40. J. Yin, L. Qi and H. Wang, Sodium titanate nanotubes as negative electrode materials for sodium-ion capacitors, ACS Appl. Mater. Interfaces 4 (2012) 2762 – 2768.

41. X. Liu, N. Zhang, J. Ni, and L. Gao, Improved electrochemical performance of sol-gel prepared $Na_4Mn_9O_{18}$ in aqueous hybrid Na-ion supercapacitor, J. Solid State Electrochem. 17 (2013) 1939 – 1944.

Table 1 The crystal structural parameters, energy gaps and the magnitude of Ni spin moments of *m*- and *t*-$NaNiPO_4$ calculated by using PBE and HSE06 functionals

Phase	Functional	a/Å	b/Å	c/Å	Volume/$Å^3$	Energy gap/ eV	Ni spin moment/μ_B
Maricite	PBE	4.97	6.67	8.83	292.41	0.76	1.577
	HSE06	4.94	6.60	8.75	285.00	4.94	1.763
Triphylite	PBE	4.98	6.13	9.98	304.23	0.86	1.544
	HSE06	4.92	6.05	9.98	297.01	5.03	1.760

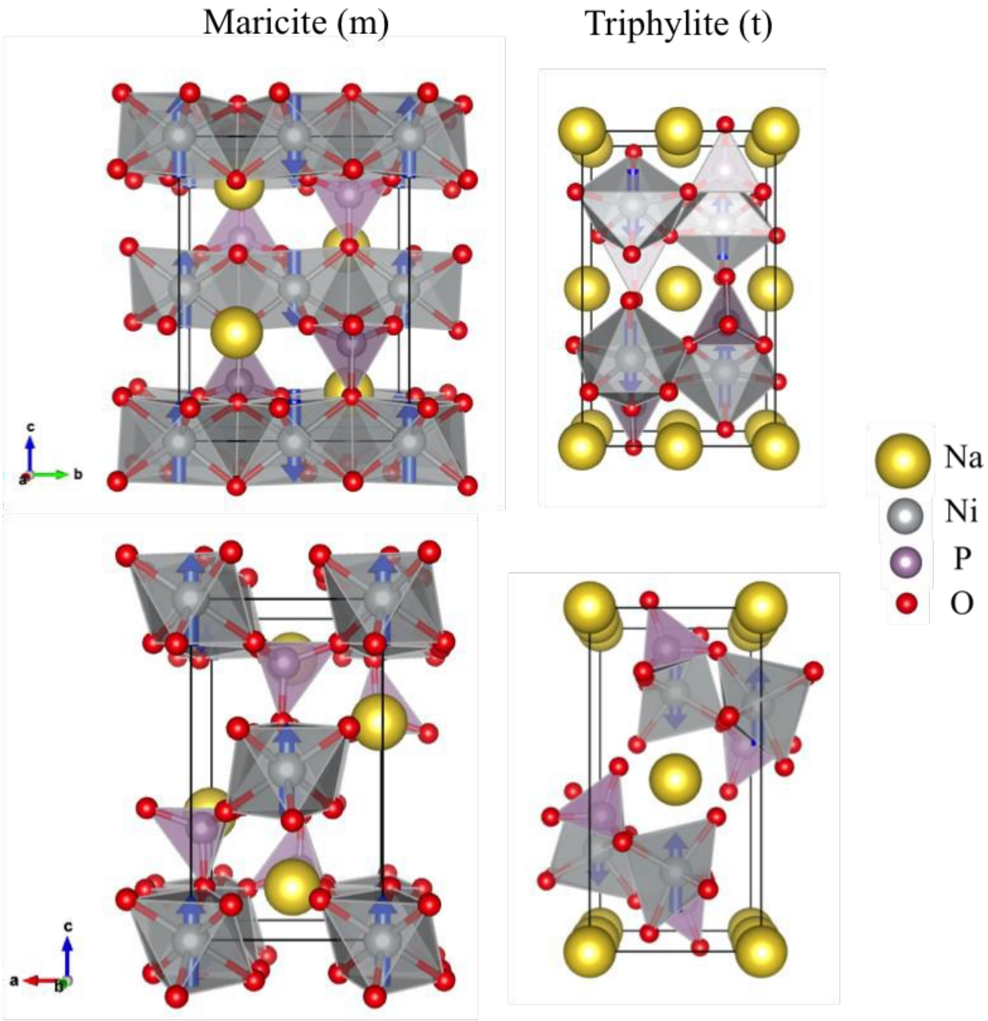

Figure 1 Crystal structures and magnetic orientation of $NaNiPO_4$ polymorphs. *m*- (left) and *t*-$NaNiPO_4$ (right) in their antiferromagnetic configurations. The Ni magnetic moments are depicted by blue arrows and are all aligned in the c-direction. The Na- diffusion channels along b-axis in triphylite is seen in the bottom representation.

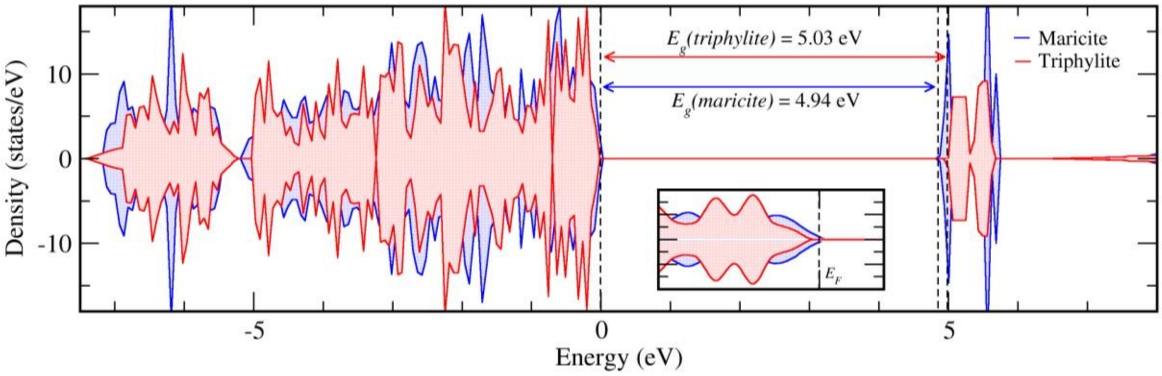

Figure 2 Total density of states of (blue line) *m*- and (red line) *t*-$NaNiPO_4$ using HSE06 functional. The Fermi levels are at 0 eV. The inset gives a higher resolution of DOS near the Fermi levels.

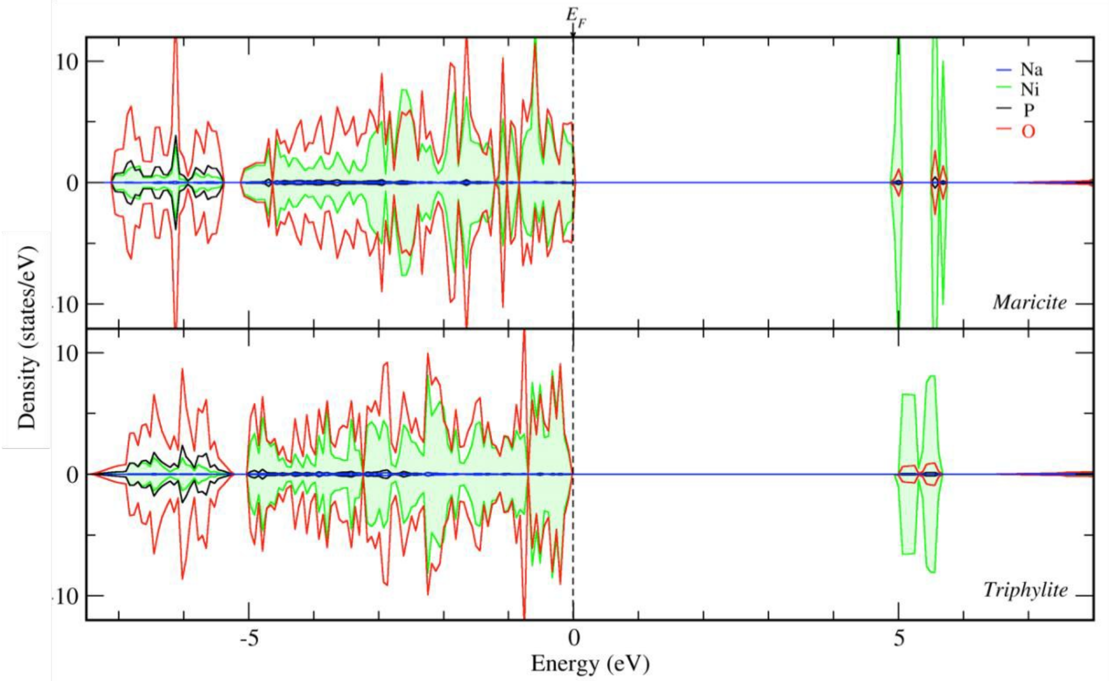

Figure 3 Projected density of states (PDOS) of (a) *m*- and (b) *t*-$NaNiPO_4$ using HSE06 functional. The Fermi levels are set at 0 eV.

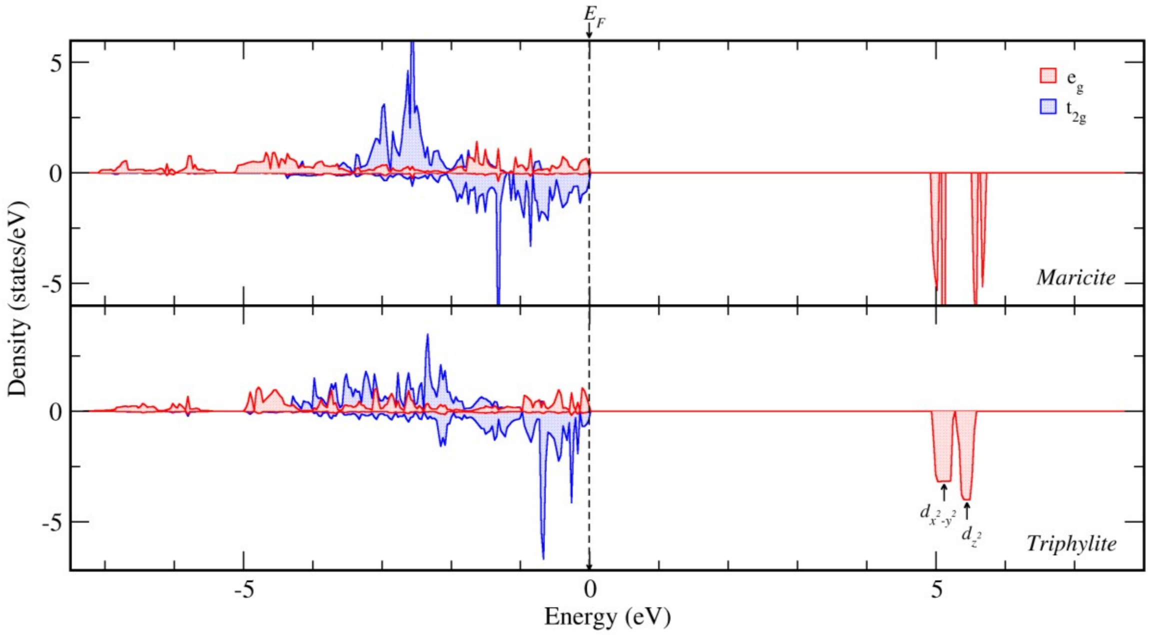

Figure 4 Projected density of states (PDOS) of 3d-Ni showing the electron occupancy in e_g (blue) and t_{2g} (red) bands under oxygen octahedral crystal fields in *m*- and *t*-$NaNiPO_4$ by using HSE06. The arrows partially specify the contributions of each e_g peak in the conduction band.

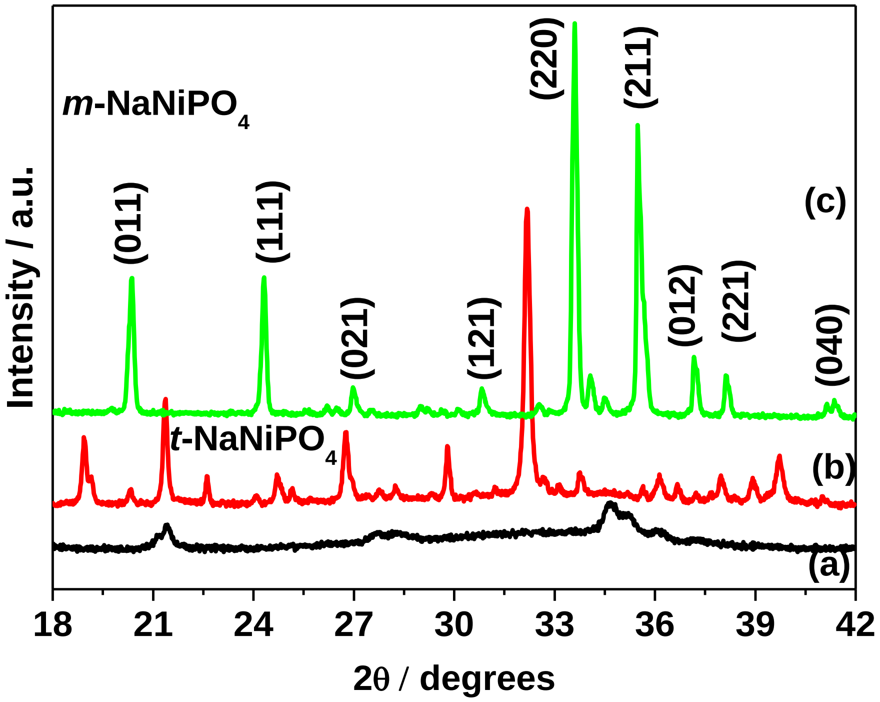

Figure 5 XRD pattern of $NaNiPO_4$ powder (a) as-prepared at 300 °C for 10 min, (b) calcined at 400 °C for 6 h, and (c) 550 °C for 6 h.

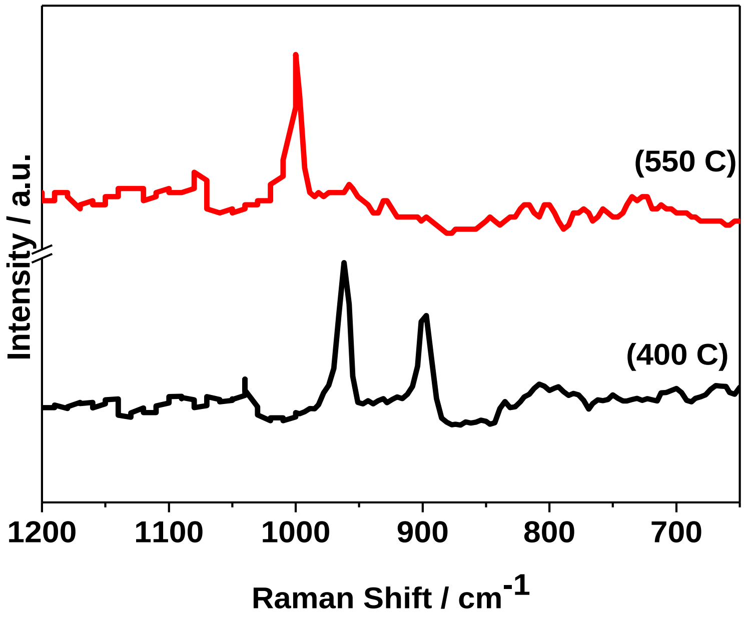

Figure 6 Raman spectra of $NaNiPO_4$ powder calcined at 400 °C and 550 °C for 6 h.

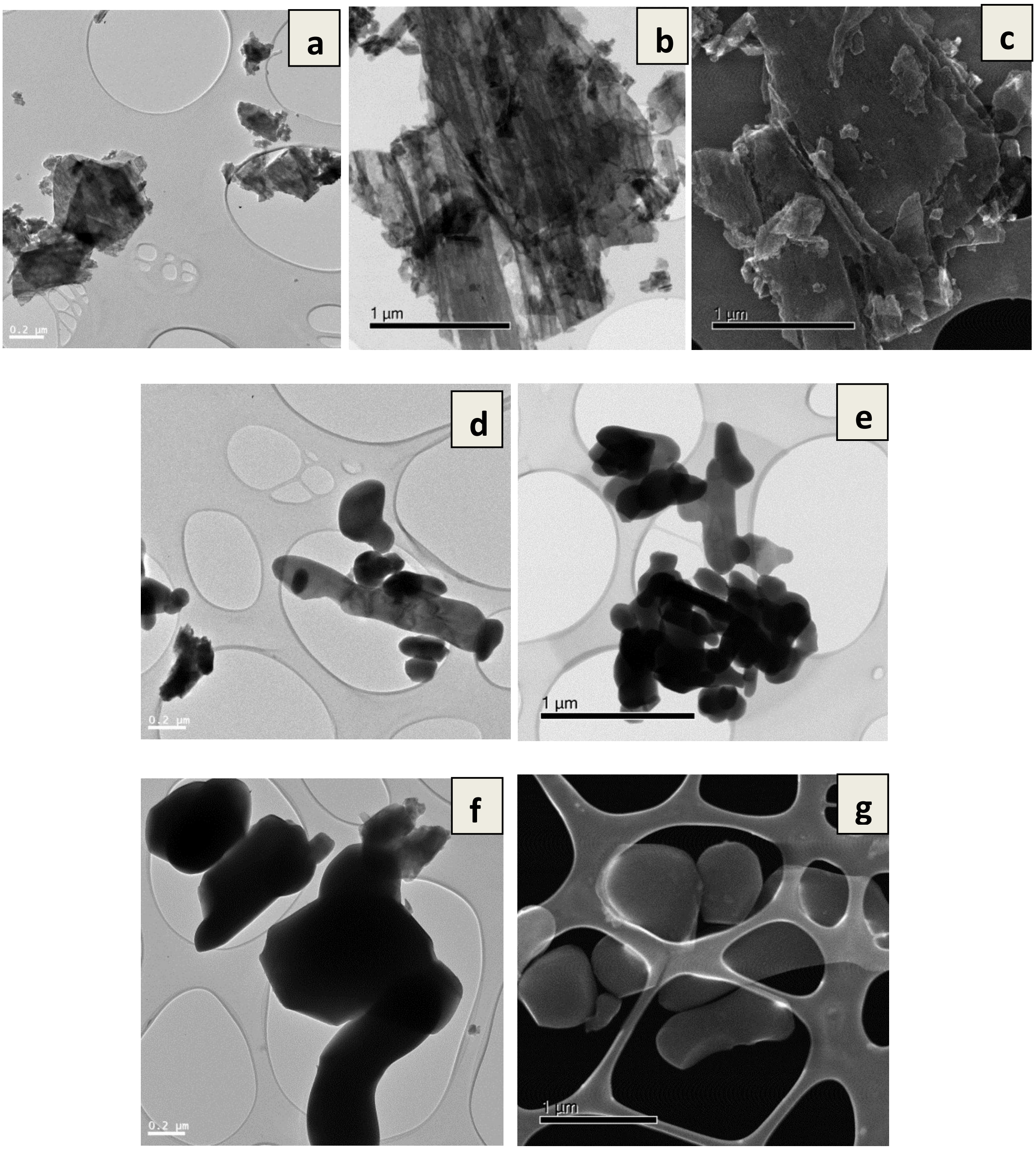

Figure 7 TEM imaging of $NaNiPO_4$ powders synthesized synthesized at (a – c) 300, (d – e) 400, and (f – g) 550 ^{o}C, respectively. (b, e) represents bright field scanning transmission electron microscopy (STEM) image. (c, g) corresponds to STEM secondary electron mode.

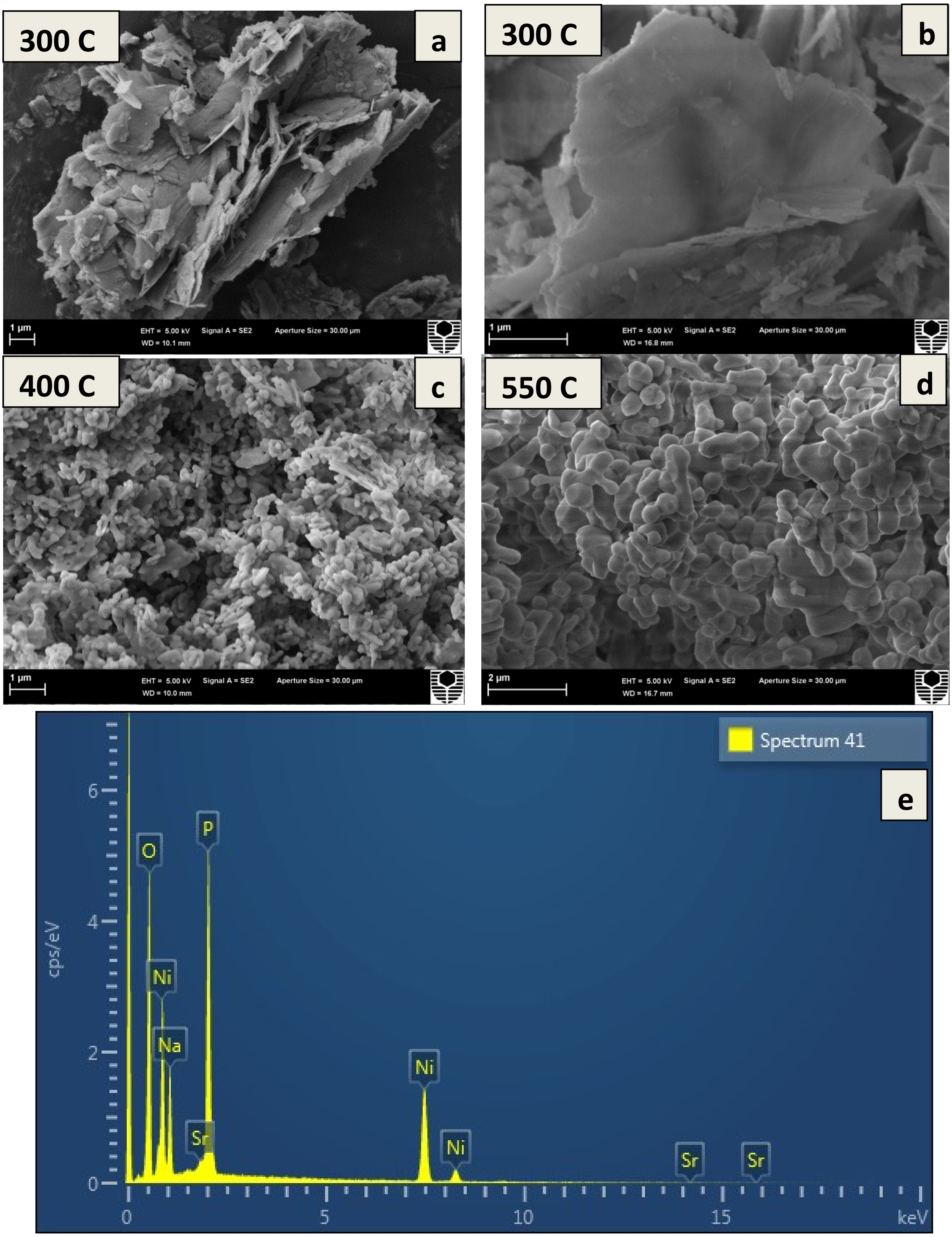

Figure 8 Field emission scanning electron microscope images of $NaNiPO_4$ powders. (a – b) low and high magnification of as-prepared $NaNiPO_4$ synthesized at 300 °C, (c –d) synthesized at 400 and 550 °C, respectively. (e) a representative EDS spectrum of $NaNiPO_4$ synthesized at 300 °C.

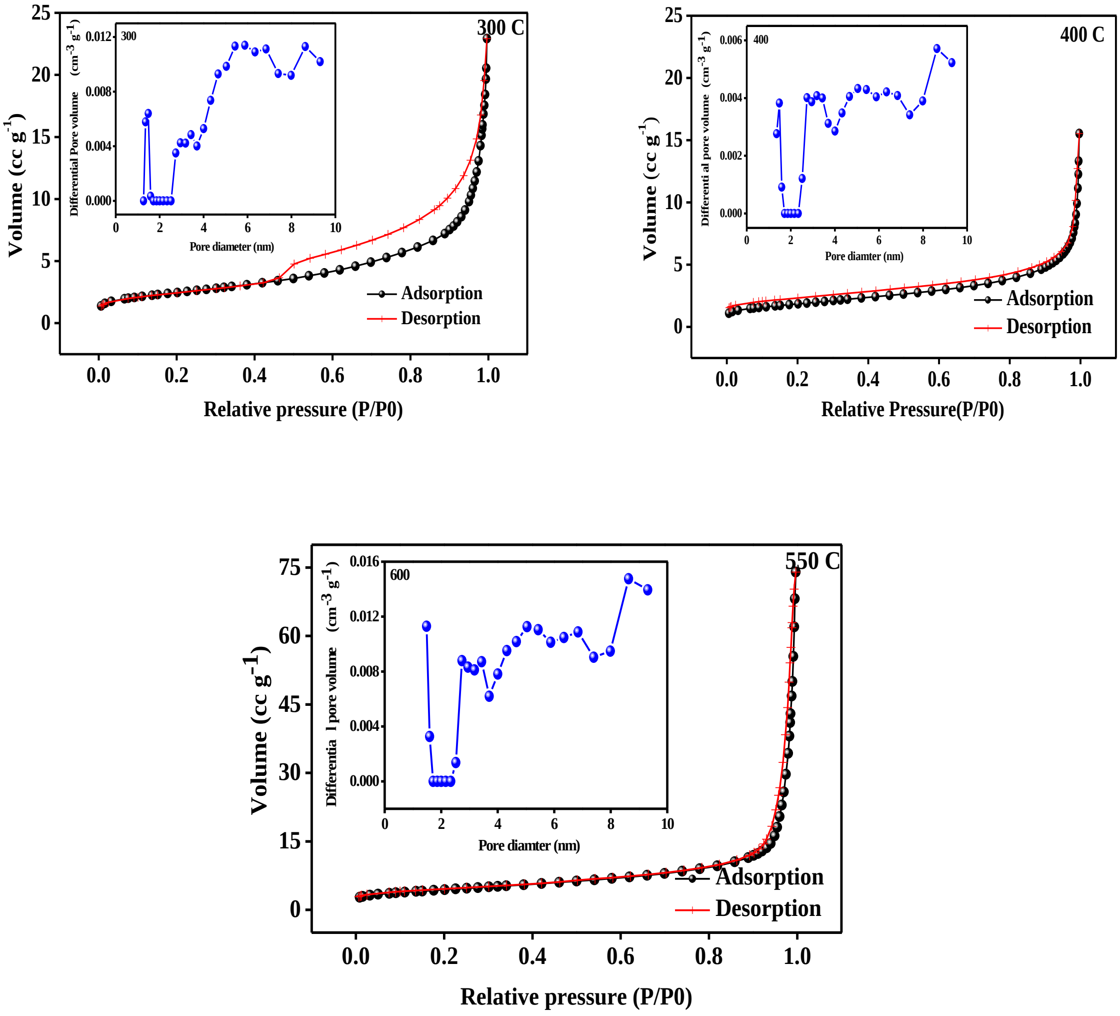

Figure 9 Nitrogen adsorption/desorption isotherms and BJH pore size distributions (inset) of $NaNiPO_4$ powders synthesized synthesized at 300, 400 and 550 ^{o}C.

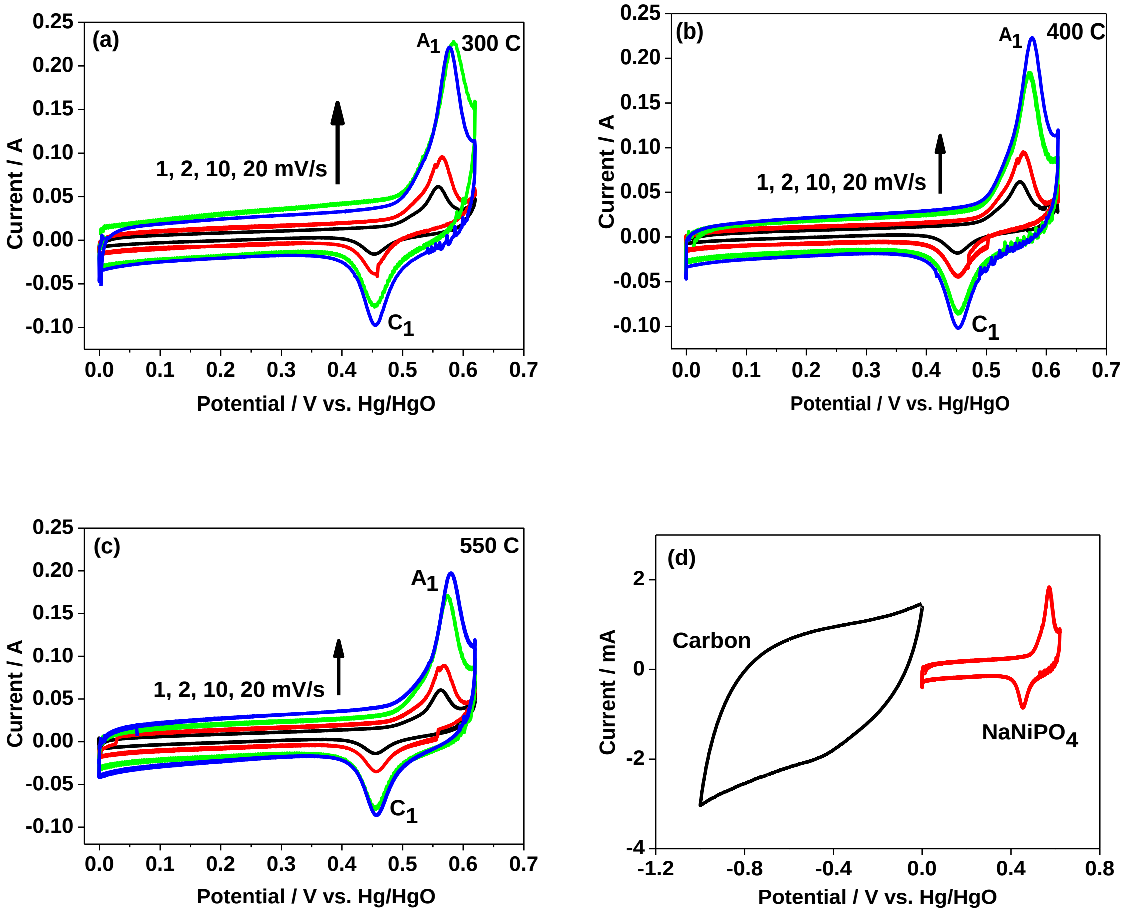

Figure 10 (a-c) Cyclic Voltammogram (CV), reduction – oxidation behavior of $NaNiPO_4$ electrodes synthesized at 300, 400 and 550 °C, respectively at sweep rates (mV s^{-1}) noted in the figure; (d) evaluation of a activated carbon (AC) negative electrode and $NaNiPO_4$ positive electrode at 2 mV/s.

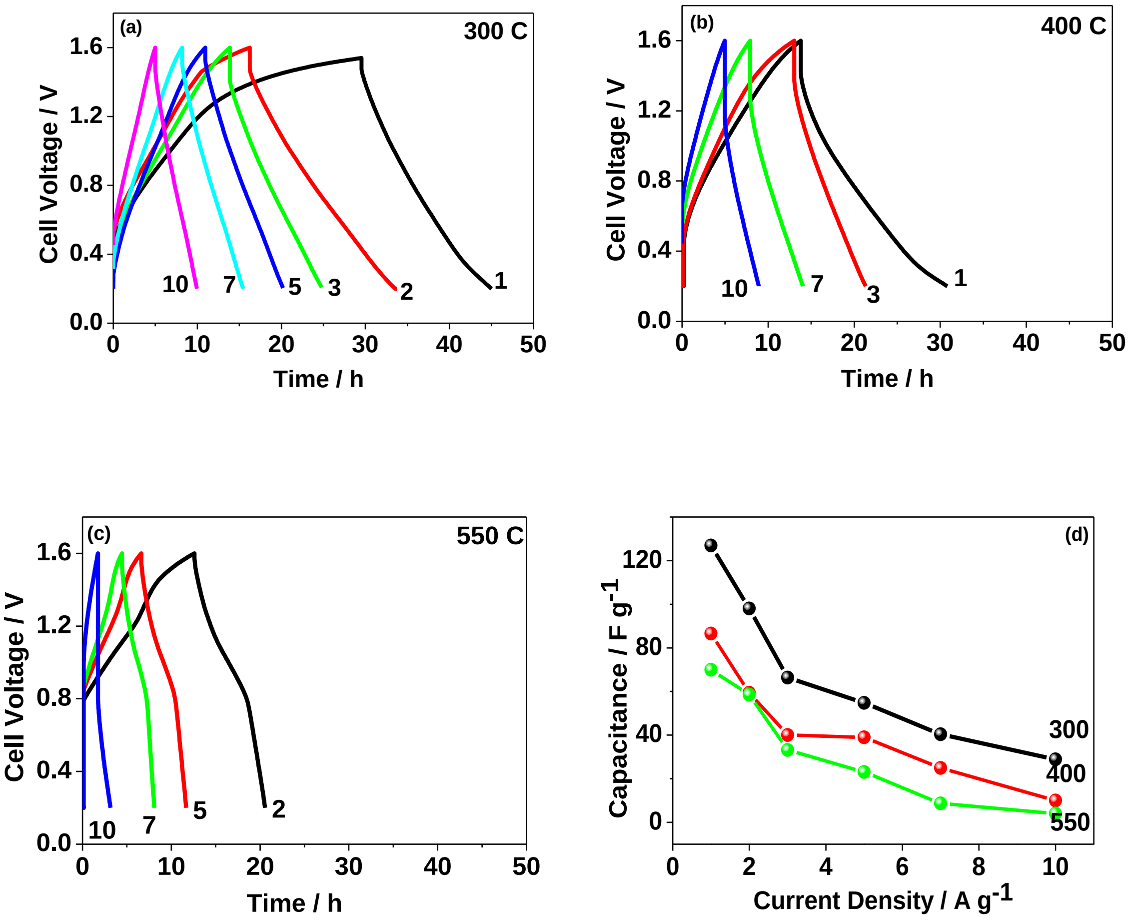

Figure 11 (a-c) Charge-discharge behavior of $NaNiPO_4$ electrodes synthesized at 300 °C, 400 and 550 °C, respectively at different current densities (A g^{-1}) noted in the figure; (d) specific capacitance as a function of current density.

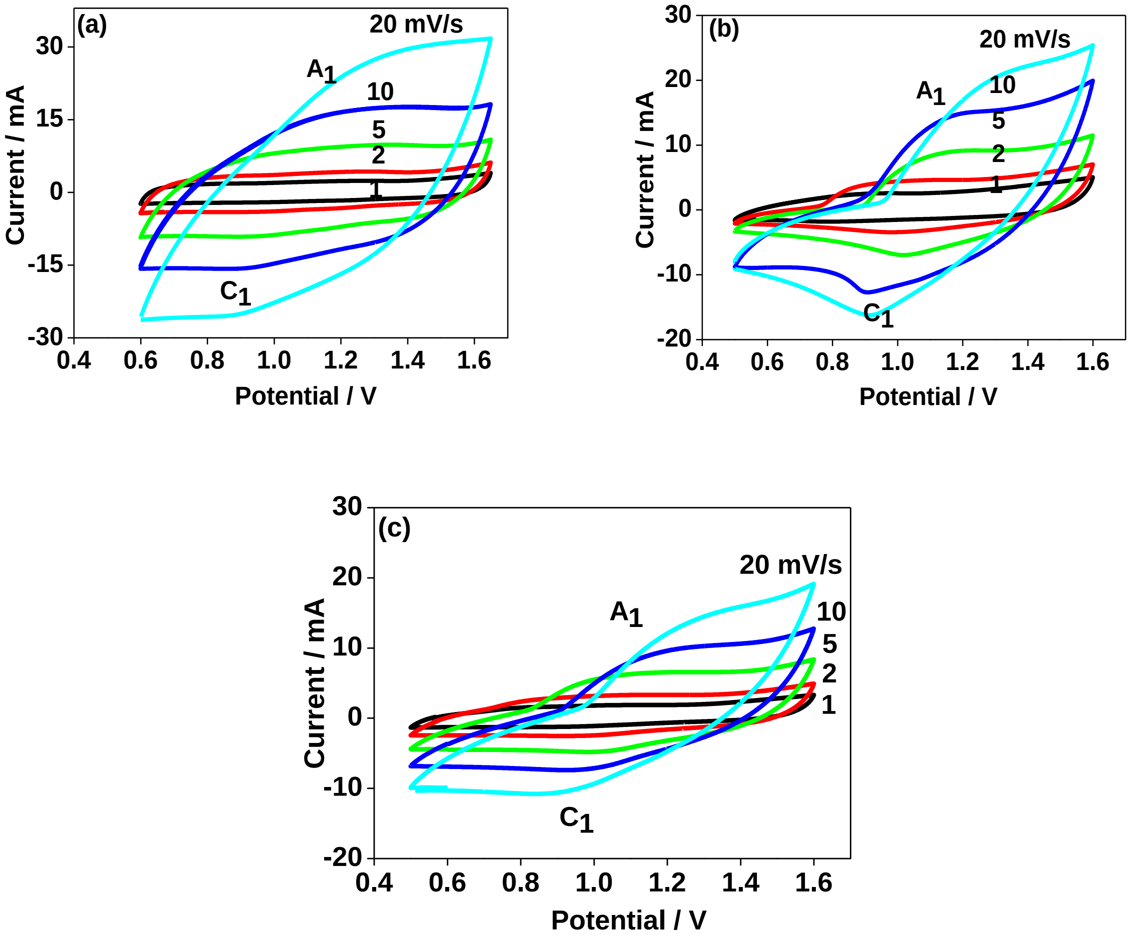

Figure 12 (a-c) Cyclic voltammetric curves (two-cell configuration) of asymmetric capacitor AC||$NaNiPO_4$ electrodes synthesized at 300, 400 and 550 ^{o}C, respectively at sweep rates (mV s^{-1}) indicated in the figure in 2 M NaOH electrolyte. Reported potential is with respect to activated carbon (AC).

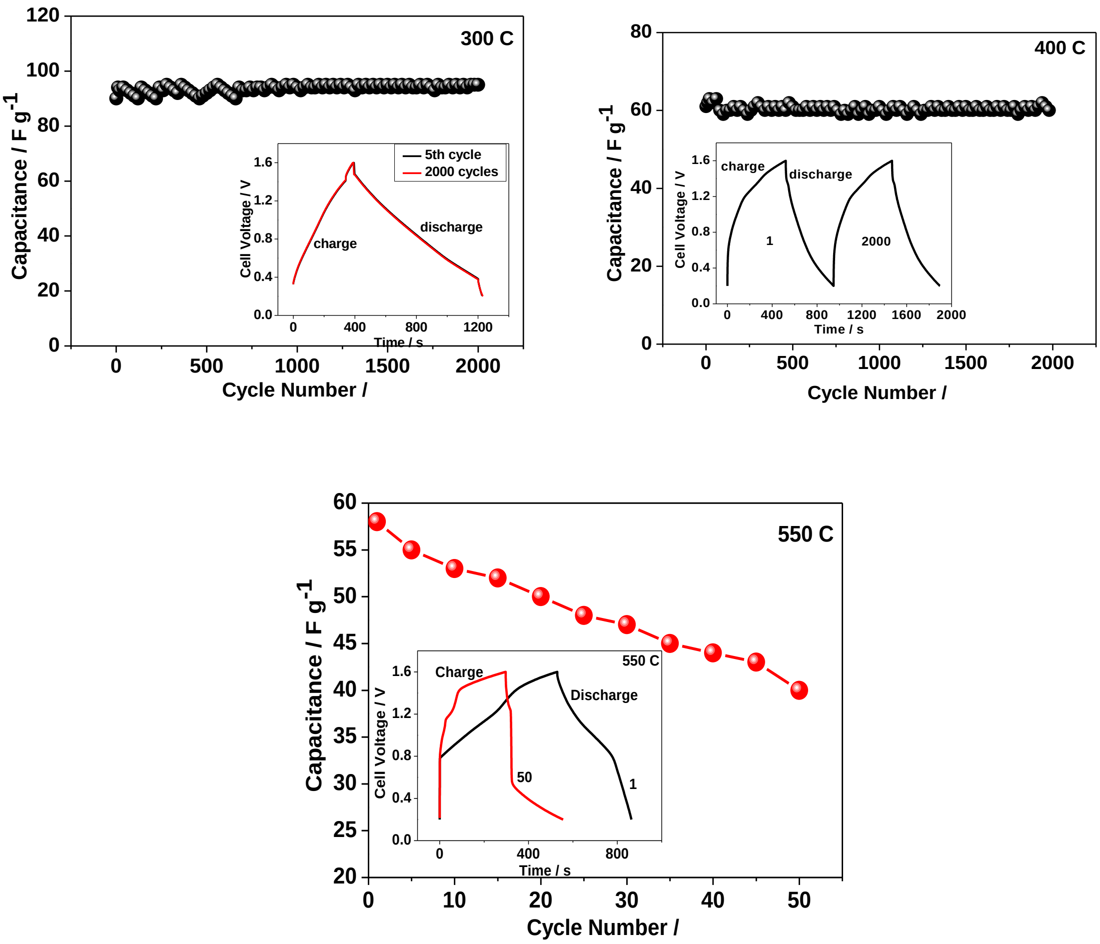

Figure 13 Cycling performances of $NaNiPO_4$ electrodes synthesized at temperatures noted in the figure. Inset shows the typical charge-discharge behavior of the initial and final cycles.

Table 2 Specific capacitance of the asymmetric capacitor AC||$NaNiPO_4$ obtained through galvanostatic charge-discharge studies at different current densities

Current density (A g^{-1})	**Specific Capacitance of $NaNiPO_4$ synthesized at 300 °C ($F g^{-1}$)**	**Specific Capacitance of $NaNiPO_4$ synthesized at 400 °C ($F g^{-1}$)**	**Specific Capacitance of $NaNiPO_4$ synthesized at 550 °C ($F g^{-1}$)**
1	**125**	**85**	**70**
2	**98**	**60**	**55**
3	**66**	**40**	**33**
5	**54**	**38**	**23**
10	**30**	**10**	**4**

Table 3 Specific capacitance of the asymmetric capacitor AC||$NaNiPO_4$ materials obtained through potentiodynamic method at different sweep rates

Scan rate (mVs^{-1})	**Specific Capacitance of $NaNiPO_4$ synthesized at 300 °C ($F g^{-1}$)**	**Specific Capacitance of $NaNiPO_4$ synthesized at 400 °C ($F g^{-1}$)**	**Specific Capacitance of $NaNiPO_4$ synthesized at 550 °C ($F g^{-1}$)**
1	**159**	**105**	**92**
2	**124**	**90**	**79**
5	**85**	**67**	**48**
10	**62**	**41**	**35**
20	**52**	**33**	**19**

Electronic Supplementary Information (ESI)

Synthesis, structural and electrochemical properties of sodium nickel phosphate for energy storage devices

Manickam Minakshi[1,*] **David Mitchell**[2]**, Rob Jones, and Feraih Alenazey**
[1]*School of Engineering and Information Technology, Murdoch University, Murdoch, WA 6150,* ***Australia***
[2]*Electron Microscope Centre, Australian Institute for Innovative Materials, Innovation Campus, University of Wollongong, North Wollongong, NSW 2500,* ***Australia***
[3]*Centre for Materials and Surface Science, La Trobe University, Bundoora, VIC 3086,* ***Australia***

[4]*Energy Research Institute, King Abdulaziz City for Science and Technology, Riyadh 11442,* **Saudi Arabia**

Teeraphat Watcharatharapong, Sudip Chakraborty, and Rajeev Ahuja
Department of Physics and Astronomy, Uppsala University, ***Sweden***

Role of Carbon (acetylene) black / PVDF in the sodium nickel phosphate cathode

To ensure good electron transport and efficient electrochemical reactions in the sodium nickel phosphate cathode, the effect of carbon (acetylene) black as a conductive carbon with various weight percent (wt. %) in the $NaNiPO_4$ cathode has been investigated. The lowest capacitance is found in the electrode that does not contain any acetylene black as additive. For the cells with 5, 10 and 15 wt. % additive, the specific discharge capacitance increased in accordance with a maximum of 125 F g^{-1}, while for the cells > 15 wt. % the available capacitance starts to decrease to 118 F g^{-1}. Hence, the role of acetylene black provides a continuous pathway for electron transport in the phosphate matrix that increases the electrical conductivity of the $NaNiPO_4$ and also aids in particle-to-particle contact enabling the charge transfer and enhancing the adsorption/desorption characteristics [1-2]. However, the optimum weight percent is found to be 15 wt. % above which the available active material decreases and also weakening the conductive network led to a less mechanical strength, hence the obtained lower capacitance. It is therefore not of much interest. Although the content of acetylene black played a vital role but the contribution of polyvinylidene difluoride (PVDF) as a polymer binder towards capacity improvement is relatively invariant. In one of our earlier studies [3] we have reported a detailed study on the effect of cathode binder on cell capacity and the study concluded that polytetrafluoroethylene (PTFE) as a binder has an impact through the formation of LiF but PVDF has no significant role. Based on this, for all our studies reported here, we have chosen the composition of acetylene black 15 wt. % and PVDF 10 wt. % in the cathode $NaNiPO_4$ composite.

Supplementary Figures

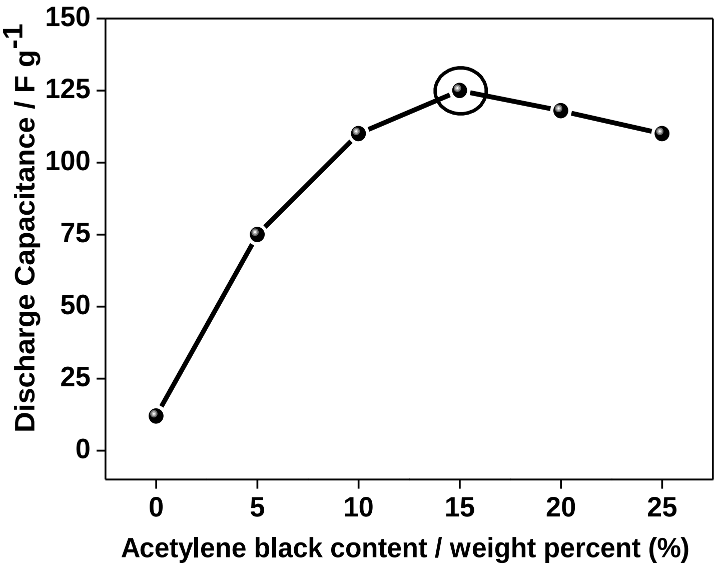

Figure S1 The discharge capacitance of $NaNiPO_4$ at various amounts of acetylene black.

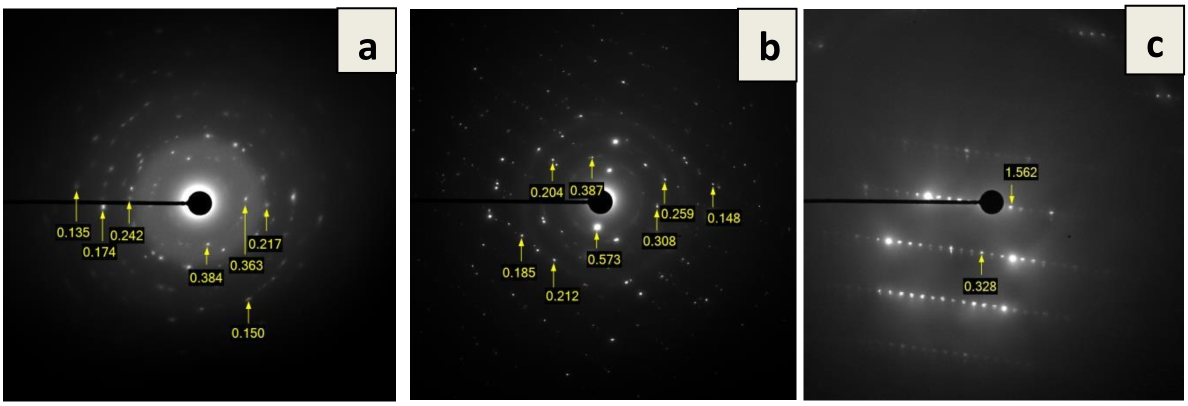

Figure S2 Selected area diffraction patterns (SADP) of $NaNiPO_4$ powders synthesized synthesized at (a) 300, (b) 400, and (c) 550 °C, respectively.

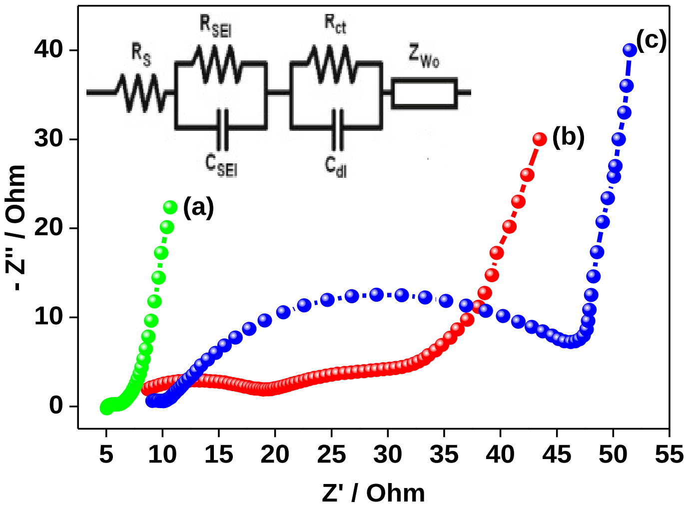

Figure S3 Nyquist plots for the asymmetric capacitor AC|$NaNiPO_4$ obtained by the electrochemical impedance spectroscopy. The $NaNiPO_4$ electrodes synthesized at 300 °C, 400 and 550 °C are shown in (a), (b) and (c) respectively. The inset shows the equivalent circuit.

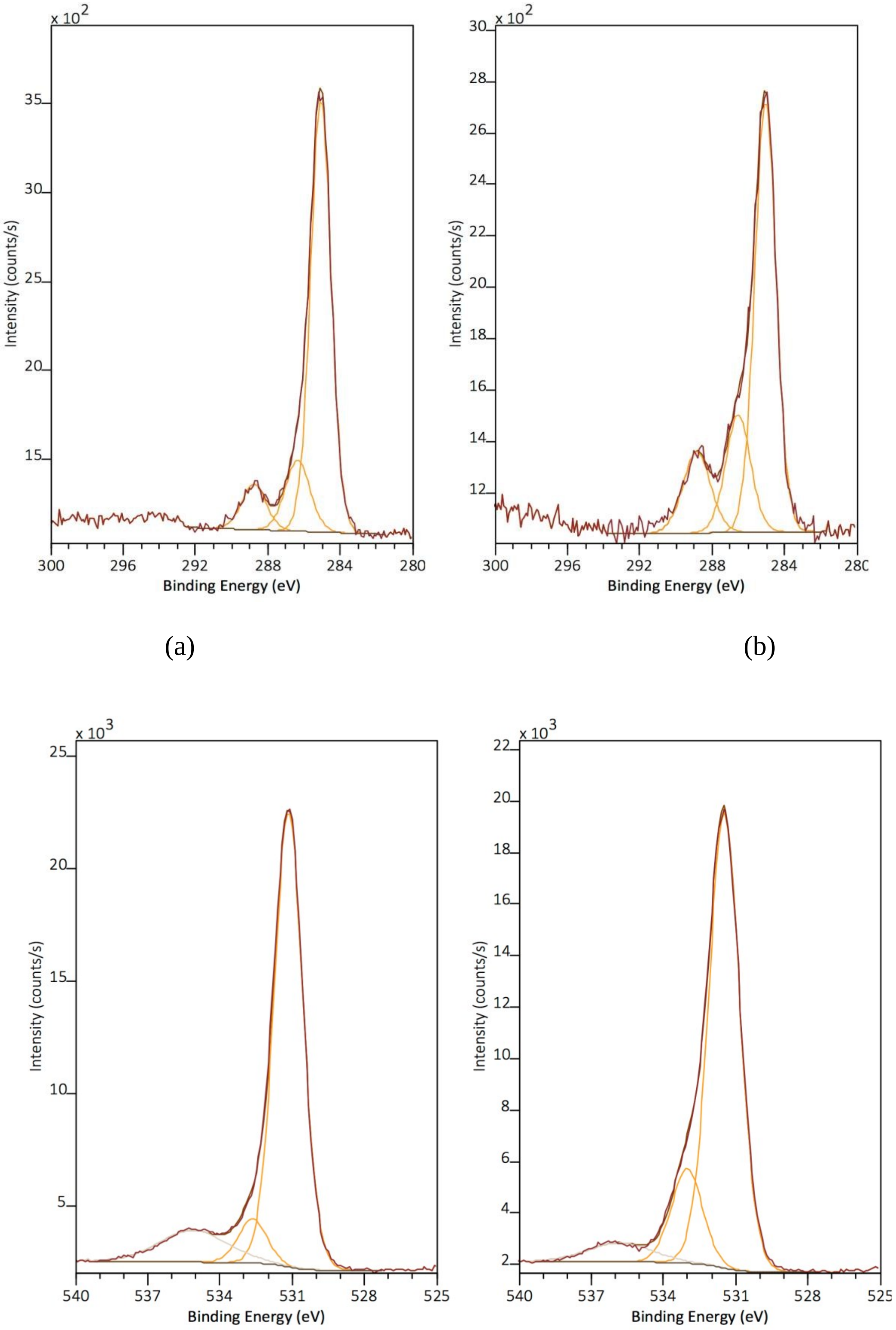

(a) (b)

(c) (d)

Figure S4 X-ray photoelectron spectroscopy (XPS) spectra of C 1s (a – b) and O 1s (c –d) for $NaNiPO_4$ samples synthesized at temperatures 400 and 500 ^{o}C respectively.

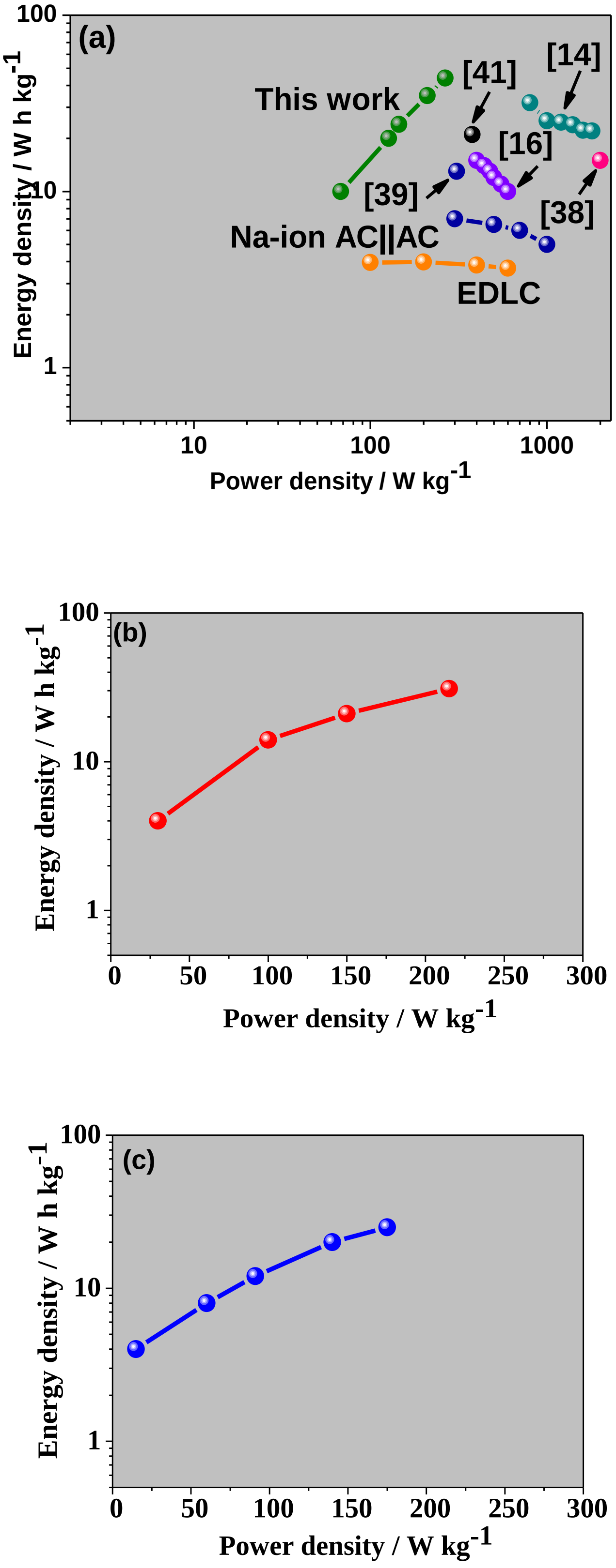

Figure S5 Ragone plot for $NaNiPO_4$ electrodes synthesized at 300 °C, 400 and 550 °C are shown in (a), (b) and (c) respectively.

Table S1 Atomic fractions of the elements detected by XPS analyses of the $NaNiPO_4$ materials synthesized at different temperatures and the relative contributions of components fitted to the C 1s and O 1s spectra.

Temperature (°C)	Atom Fractions (%)										
	Elements						C 1s components			O 1s components	
	Na	Ni	P	O	C	N	C–C	C–O	O=C–O	Inorganic	Organic
300	6.7	14.1	10.9	49.6	15.4	3.3	68.4	19.4	12.2	78.2	21.8
400	12.5	11.5	11.1	49.2	15.7	-	75.4	15.0	9.6	91.6	8.4
550	8.5	14.9	11.2	50.7	12.6	2.1	65.1	20.3	14.6	84.1	15.9

References

1. J. Wang, J.-Z. Wang, Z.-Q. Sun, X.-W. Gao, C. Zhong, S.-L. Chou and H.-K. Liu, A germanium/single-walled carbon nanotube composite paper as a free-standing anode for lithium-ion batteries, J. Mater. Chem. A 2 (2014) 4613 – 4618.
2. M. Manickam and M. Takata, Electrochemical and X-ray photoelectron spectroscopy studies of carbon black as an additive in Li batteries, J. Power Sources 112 (2002) 116 – 120.
3. M. Manickam and M. Takata, Effect of cathode binder on capacity retention and cycle life in transition metal phosphate of a rechargeable lithium battery” Electrochim. Acta 48 (2003) 957 – 963.